

Epigenetic state inheritance drivers drug-tolerant persister-induced resistance in solid tumors: A stochastic agent-based model

Xiyin Liang and Jinzhi Lei

School of Mathematical Sciences, Center for Applied Mathematics,
Tiangong University, Tianjin, 300387, China.

*Corresponding author(s). E-mail(s): jzlei@tiangong.edu.cn;
Contributing authors: liangxiyin@tiangong.edu.cn;

Abstract

The efficacy of anti-cancer therapies is severely limited by the emergence of drug resistance. While genetic drivers are well-characterized, growing evidence suggests that non-genetic mechanisms, particularly those involving drug-tolerant persisters (DTPs), play a pivotal role in solid tumor relapse. To elucidate the evolutionary dynamics of DTP-induced resistance, we develop a stochastic agent-based model (ABM) of solid tumor evolution that couples macroscopic population dynamics with microscopic epigenetic state inheritance during the cell cycle. Our simulations accurately reproduce the temporal progression of relapse observed in experimental studies, capturing the dynamic transition from sensitive cells to DTPs, and ultimately to stable resistant phenotypes under prolonged therapy. By explicitly modeling the epigenetic plasticity of individual cells, our model bridges the gap between cellular heterogeneity and population-level tumor evolution. Furthermore, we performed *in silico* clinical trials using virtual patient cohorts to evaluate therapeutic outcomes, demonstrating that optimized adaptive treatment strategies can significantly delay tumor relapse compared to standard dosing. This study provides a quantitative framework for dissecting DTP-driven resistance mechanisms and designing more effective, biologically informed therapeutic strategies.

Keywords: cell plasticity, drug-tolerant persister cells, drug resistance, agent-based model

1 Introduction

Over the past decades, targeted therapies have significantly improved the survival of cancer patients. However, drug resistance remains the greatest challenge to achieving durable remission or cure. While classical evolutionary theories have predominantly focused on genetic drivers (e.g., pre-existing or *de novo* mutations), growing evidence indicates that non-genetic mechanisms play a critical role in mediating drug resistance in solid tumors, particularly during the initial phase of treatment (Boumahdi and de Sauvage 2020; McDonald and Dedhar 2024; Calderon et al. 2024). Understanding how these non-genetic adaptive strategies drive tumor relapse is therefore essential for designing more effective therapeutic schedules.

A key contributor to non-genetic resistance is the emergence of drug-tolerant persistor cells (DTPs) (Bell and Gilan 2020; McDonald and Dedhar 2024). The phenomenon of drug tolerance, originally characterized in bacterial populations as ‘persistence’ (Balaban et al. 2019), implies a transient state of multidrug tolerance that is not encoded by genetic mutations. DTPs have been observed across multiple cancer types, including non-small cell lung cancer (NSCLC) (Sharma et al. 2010), melanoma (Rambow et al. 2018), colorectal cancer (CRC) (Rehman et al. 2021), and glioblastoma (Liau et al. 2017). Importantly, DTPs exhibit distinct dynamics under short- versus long-term treatments. For example, in NSCLC PC9 cells treated with erlotinib, a small fraction of cells survive in a slow-cycling state and revert to drug sensitivity upon drug withdrawal (Sharma et al. 2010). However, under prolonged exposure, these cells eventually evolve into stably resistant populations.

The molecular basis of DTPs involves complex intracellular rewiring. Multiple processes, including chromatin remodeling, metabolic reprogramming, and activation of alternative signaling pathways, have been implicated in the emergence and maintenance of DTPs. For instance, cancer cells exposed to stress can generate a reversible DTP population characterized by upregulation of IGF-1R, CD133, and KDM5A (Sharma et al. 2010). IGF-1R signaling is required for the establishment of drug tolerance, which is associated with distinct chromatin states that can be disrupted pharmacologically. Several signaling pathways, such as Wnt/β-catenin and Notch, have also been shown to contribute to DTP formation (Reyes et al. 2025; Arasada et al. 2018). In NSCLC, enhanced acetylcholine (ACh) metabolism promotes DTP formation by activating Wnt/β-catenin signaling (Nie et al. 2022). Moreover, stromal cells in the tumor microenvironment (TME), such as cancer-associated fibroblasts (CAFs) and tumor-associated macrophages (TAMs), secrete cytokines that further support DTP survival (Straussman et al. 2012). These findings suggest that the cell state is not a simple binary switch (sensitive vs. resistant) but rather a high-dimensional continuous phenotype modulated by microenvironment cues and epigenetic regulators.

Mathematical modelling has proven effective in decoding these complex evolutionary dynamics. Several approaches have provided insights into the trade-offs between cell kill and tolerance induction. Classical ordinary differential equation (ODE) models typically stratify cell populations into discrete compartments (e.g., sensitive, tolerant, resistant) to study transition rates and dosage optimization (Kuosmanen et al. 2021; Gevertz et al. 2025). More recent works have employed optimal control theory

to balance toxicity and resistance suppression (Fischer and Blüthgen 2024; Gunnarsson et al. 2025). To capture spatial heterogeneity, partial differential equation (PDE) models have been employed to study the role of the tumor microenvironment in resistance (Zheng et al. 2018). Furthermore, agent-based lineage models have been developed to infer resistance dynamics by integrating single-cell data, offering higher resolution on the timing of DTP emergence (Iyer et al. 2025; Whiting et al. 2025; Wang et al. 2025). Notably, Chisholm et al. proposed coupled individual-based and integro-differential equation models to study reversible phenotypic evolution under cytotoxic drug exposure, demonstrating how adaptation within non-genetically unstable populations drives the outgrowth of proliferative resistant clones (Chisholm et al. 2015).

However, most existing frameworks rely on mean-field approximations or discrete-state assumptions, which may overlook a defining feature of DTPs: the “resistance continuum” (Feinberg and Levchenko 2023). Experimental data from single-cell RNA sequencing reveal that acquired resistance involves a series of gradual cell-state transitions driven by intracellular epigenetic variations (França et al. 2024). Crucially, these epigenetic states are inherited with noise during cell division, creating a “memory” effect that standard ODEs fail to capture (Probst et al. 2009). Therefore, a framework that explicitly integrates microscopic epigenetic inheritance with macroscopic population dynamics is necessary to elucidate how continuous phenotypic drift drives relapse.

In this study, we develop a stochastic agent-based model (ABM) specifically calibrated for NSCLC treatment. Theoretically grounded in the stochastic inheritance framework proposed by Lei (Lei 2020b), our model instantiates the cell state as a continuous vector coupling drug sensitivity with stemness. By defining an inheritance probability kernel, we explicitly model how epigenetic phenotypes are passed from mother to daughter cells with varying degrees of fidelity. This multiscale approach allows us to: (1) reproduce the temporal progression from reversible tolerance to irreversible resistance; (2) quantify how epigenetic plasticity induces DTP-mediated resistance; and (3) conduct *in silico* clinical trials using virtual patient cohorts to identify adaptive therapy strategies that significantly prolong progression-free survival.

2 Models and Methods

Tumors are characterized by uncontrolled cellular proliferation. Here, we propose a multi-scale mathematical model, based on stem cell regeneration dynamics, to quantify the evolutionary dynamics of tumor relapse under targeted therapy. While the population dynamics are formally governed by an integro-differential equation (IDE) (derived in Appendix A), we permit a high-dimensional representation of cell states by implementing the model as a stochastic agent-based model (ABM). In this section, we first outline the biological rules and structure of the ABM, followed by a detailed definition of the epigenetic state variables and kinetic rates. Finally, we provide the parameter estimation strategy based on experimental benchmarks.

2.1 Model description

To capture the interplay between cell cycle progression and phenotypic plasticity, our model is built upon the heterogeneous stem cell regeneration framework established by Lei (Lei 2020a,b). As illustrated in Fig. 1A, the cell cycle is partitioned into two distinct phases: a resting phase (G0) and a proliferative phase. The life cycle of an individual cell is governed by the following stochastic rules:

- Resting phase (G0): Cells in the G0 phase can either re-enter the cell cycle at a proliferation rate β or exit the population at a removal rate κ , which aggregates the effects of terminal differentiation, senescence, and death.
- Proliferative phase: Once in the cell cycle, cells undergo a fixed duration τ of preparation. During the period, they are subject to apoptosis at a rate μ . Surviving cells divide into two daughter cells, which immediately return to the G0 phase to begin a new cycle.

We consider target therapy using EGFR-TKIs, such as erlotinib and osimertinib, which are primarily cytostatic agents rather than cytotoxic ones. They work by blocking the growth signaling pathway and interfering with the inheritance of epigenetic states, rather than directly increasing apoptosis.

To elucidate the molecular mechanism of DTP-induced resistance, we characterized each cell by a multidimensional epigenetic state vector \mathbf{x} , rather than discrete phenotypic labels. As shown in Fig. 1A, the variation in \mathbf{x} dictates cellular heterogeneity, directly modulating the kinetic rates β , κ , and μ . Crucially, phenotypic plasticity arises from the stochastic inheritance of \mathbf{x} during mitosis. Due to the molecular complexity of chromatin remodeling, we do not model specific pathways but instead describe this “memory loss” or “rewiring” via a phenomenological inheritance probability kernel, $p(\mathbf{x}, \mathbf{y})$. This kernel defines the probability density that a mother cell with state \mathbf{y} produces a daughter cell with state \mathbf{x} , thereby coupling microscopic epigenetic drift with macroscopic population evolution.

The schematic diagram of the stochastic simulation algorithm is presented in Fig. 1B. This ABM approach allows us to track the lineage and trajectory of rare persister cells, which is computationally prohibitive in grid-based numerical methods for high-dimensional IDE. Specific details of the simulation algorithm are provided in Section 2.2.

2.1.1 Epigenetic states and cell phenotypes

Biological evidence suggests that acquired resistance is not a binary switch but a dynamic remodeling process driven by transcriptional plasticity. In an experimental work by Sharma et al. (2010), PC9 NSCLC cells treated with erlotinib exhibited a transient drug-tolerant state (DTPs) associated with the loss of EGFR signaling and the upregulation of stemness markers (e.g., CD133, CD44) and IGF-1R. Under prolonged exposure, these cells eventually evolved into stably resistant colonies (DRCs), often characterized by the activation of alternative pro-survival pathways (e.g., increased acetylcholine metabolism or Wnt signaling) to bypass EGFR inhibition (Nie et al. 2022; Reyes et al. 2025).

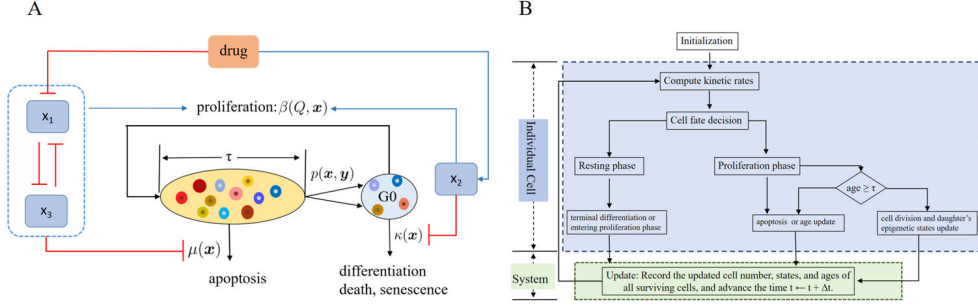


Fig. 1 Schematic of the multi-scale theoretical framework and the agent-based simulation flow. **A** The heterogeneous stem cell regeneration model. Tumor dynamics follow a G0 cell cycle structure where kinetic rates depend on the cell’s epigenetic state $\mathbf{x} = (x_1, x_2, x_3)$. $Q(t, \mathbf{x})$ represents the density of G0 cells with state \mathbf{x} . The orange region denotes the proliferative phase (duration τ). Cellular plasticity is mathematically captured by the inheritance probability kernel $p(\mathbf{x}, \mathbf{y})$, describing how epigenetic states are transmitted with variation from mother (\mathbf{y}) to daughter (\mathbf{x}). Colored circles within blue and orange regions represent cells with varying phenotypes. The lines with red bars denote inhibition, while blue arrows indicate promotion, and black arrows represent cell transition. **B** Flowchart of the agent-based stochastic simulation. The system is initialized with all cells in the resting phase. At each time step, the probabilities of cell fate decisions (division, death, differentiation) are computed for each agent based on its state \mathbf{x} . Detailed implementations are provided in Section 2.2.

Epigenetic states

To formulate the biological complexities into a tractable mathematical framework, we reduce the high-dimensional molecular profile of a cell as a three-dimensional epigenetic state vector $\mathbf{x} = (x_1, x_2, x_3) \in \Omega \subset \mathbb{R}^3$. These three components correspond to the distinct functional axes of resistance evolution:

1. Drug sensitivity (x_1): Represents the activity of the primary oncogenic drivers (e.g., EGFR pathway and downstream ERK/AKT signaling) targeted by the drug.
2. Stemness/Plasticity (x_2): Quantifies the differentiation potential. High levels of x_2 indicate a slow-cycling, stem-like state characteristic of DTPs. Biologically, x_2 serves as a proxy for stem cell markers such as CD133, CD44, and Oct4.
3. Alternative adaptation (x_3): Represents the activation of bypass signaling pathways that restore proliferative capacity in the presence of the drug. These signaling pathways include IGF-1R (Sharma et al. 2010). Specifically for the data used in this study (Nie et al. 2022), x_3 represents the Acetylcholine (ACh) signaling axis (measured by ACh levels or ChAT expression).

Table 1 provides a summary of the biological interpretation of these variables.

Given the state vector, $Q(t, \mathbf{x})$ represents the density of G0 cells with state \mathbf{x} , and $Q(t) = \int_{\Omega} Q(t, \mathbf{x})$ give the total number of G0 cells at time t .

Cell phenotype identification

While the underlying epigenetic state \mathbf{x} is continuous—reflecting the “resistance continuum” (França et al. 2024)—there are clinically observed distinct cell types. To

Table 1 Microscopic epigenetic state variables and their biological interpretation.

Variable	Biological interpretation
x_1	Activity of the drug-targeted pathway. Higher x_1 implies a higher growth rate but greater susceptibility to therapy.
x_2	Potential of self-renewal and plasticity. Higher x_2 induces quiescence (G0 arrest) and promotes survival (DTP state).
x_3	Activity of alternative pathways. Higher x_3 allows cells to re-enter the cell cycle despite drug inhibition.

identify cell phenotypes from the epigenetic state, we classify cells into three canonical phenotypes based on expression thresholds x_s^1 , x_s^2 , and x_s^3 (Table 2):

- DSCs (Drug-Sensitive Cells): high target expression ($x_1 > x_s^1$) and low stemness ($x_2 < x_s^2$).
- DTPs (Drug-Tolerant Persisters): low target expression ($x_1 \leq x_s^1$) but high stemness ($x_2 > x_s^2$), corresponding to a reversible, slow-cycling state.
- DRCs (Drug-Resistant Cells): low target expression ($x_1 \leq x_s^1$) and low stemness ($x_2 \leq x_s^2$), but high adaptation ($x_3 > x_s^3$), regaining proliferative capacity.

This classification allows us to map continuous simulation trajectories onto clinically recognizable stages of relapse (Fig. 2 and Table 2).

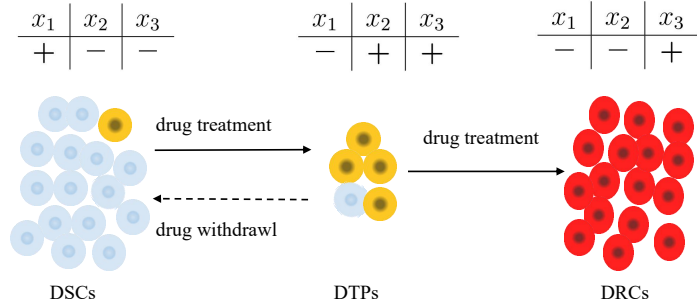


Fig. 2 Phenotypic transitions mapped on the epigenetic landscape. Before therapy, the population is dominated by DSCs (high x_1). Drug treatment suppresses x_1 , selecting for DTPs (high x_2) which survive in a dormant state. Under continuous pressure, stochastic epigenetic drift eventually accesses the high- x_3 basin, leading to the outgrowth of proliferative DRCs.

Table 2 Classification criteria for tumor cell phenotypes.

Phenotype	Active Markers	Criterion (Notation)
DSCs	$x_1^{\text{high}}, x_2^{\text{low}}$	$(x_1, x_2, x_3) \in (x_s^1, +\infty) \times (0, x_s^2] \times (0, x_s^3]$
DTPs	$x_1^{\text{low}}, x_2^{\text{high}}$	$(x_1, x_2, x_3) \in (0, x_s^1] \times (x_s^2, +\infty) \times (x_s^3, +\infty)$
DRCs	$x_1^{\text{low}}, x_2^{\text{low}}, x_3^{\text{high}}$	$(x_1, x_2, x_3) \in (0, x_s^1] \times (0, x_s^2] \times (x_s^3, +\infty)$

2.1.2 Kinetic rates

Standard constant-rate models cannot capture the adaptive landscape of resistance. Here, we assume the kinetic rates (β, μ, κ) are functionally dependent on the epigenetic state \mathbf{x} , governed by the following biological logic (illustrated in Fig. 1A):

1. Proliferation is driven by both the primary target (x_1) and alternative pathways (x_3), but is suppressed by stemness (x_2). This creates a non-monotonic dependence of proliferation on x_2 , where intermediate stemness favors expansion while extreme stemness favors dormancy.
2. There exists a reciprocal inhibition between the dominant sensitive pathway (x_1) and the adaptive pathway (x_3), reflecting the metabolic cost of switching signaling dependencies.
3. Therapeutic agents inhibit the function of x_1 , thereby reducing proliferation. However, this stress selectively favors cells with high x_2 (DTPs) or high x_3 (DRCs).

The precise mathematical formulations of these dependencies are detailed below.

Proliferation and differentiation rates

The proliferation rate β incorporates population-level feedback regulation to maintain tissue homeostasis. Biologically, the self-renewal capacity of stem cells is constrained by microenvironmental signals and available niche space. Following established theoretical frameworks (Bernard et al. 2003; Lei 2020b), we model this feedback using a phenomenological Hill function dependent on the total resting phase population $Q(t)$:

$$\beta = \beta_0(\mathbf{x}) \frac{\theta(\mathbf{x})^m}{\theta(\mathbf{x})^m + Q(t)^m},$$

where $\beta_0(\mathbf{x})$ represents the intrinsic proliferation potential at low cell density, and $\theta(\mathbf{x})$ denotes the effective carrying capacity (or characteristic cell number) at which the proliferation rate is halved.

The intrinsic proliferation rate β_0 and terminal differentiation rate κ are modulated by the stemness state x_2 . We construct these functions to reflect the biological logic of stem cells:

- High x_2 corresponds to quiescent stem cells (low proliferation, negligible differentiation);
- Intermediate x_2 represents transient amplifying cells (maximal proliferation);
- Low x_2 indicates differentiated cells (reduced proliferation, high differentiation rate).

To capture this behavior, we define $\beta_0(\mathbf{x})$ as a unimodal function of x_2 , while the differentiation rate $\kappa(\mathbf{x})$ as a monotonically decreasing function:

$$\beta_0(\mathbf{x}) = \bar{\beta} \frac{a_1 x_2 + (a_2 x_2)^4}{1 + (a_3 x_2)^4}, \quad (1)$$

$$\kappa(\mathbf{x}) = \kappa_0 \frac{1}{1 + (\kappa_1 x_2)^{n_\kappa}}, \quad (2)$$

where $\bar{\beta}$ and κ_0 characterize the maximum rates of proliferation and differentiation, respectively. The coefficients a_i , κ_1 , and Hill exponent n_κ shape the response curves, as illustrated in Fig. 3.

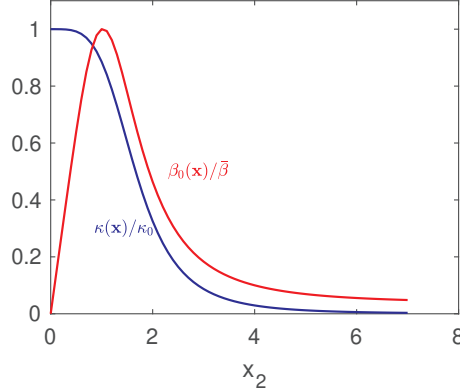


Fig. 3 Functional dependence of kinetic rates on the stemness x_2 . The proliferation rate $\beta_0(\mathbf{x})$ (red curve, normalized by $\bar{\beta}$) exhibits a unimodal profile, peaking at intermediate x_2 values (progenitor state) and decreasing at high x_2 (quiescent stem state). The differentiation rate $\kappa(\mathbf{x})$ (blue curve, normalized by κ_0) decreases monotonically with increasing stemness.

The parameter θ is regulated by drug sensitivity (x_1) and adaptive resistance (x_3). We assume these two pathways act explicitly to promote survival and growth signaling. The effective carrying capacity parameter θ is defined as:

$$\theta(\mathbf{x}) = \theta_0 \left(1 + a_5 \frac{(a_4(x_1 + \alpha x_3))^6}{1 + (a_4(x_1 + \alpha x_3))^6} \right), \quad (3)$$

where θ_0 is the basal level, and the term in the parentheses describes the saturation effect of oncogenic signaling ($x_1 + \alpha x_3$). Here, α weights the relative contribution of the adaptive pathway x_3 compared to the primary target x_1 .

Apoptosis rate

Similar to the parameter θ , the apoptosis rate μ is also jointly regulated by drug sensitivity (x_1) and adaptive resistance (x_3) through the oncogenic signaling ($x_1 +$

αx_3). Thus, we model μ as an exponentially decaying function of the combined survival signals:

$$\mu(x_1, x_3) = \mu_0 e^{\mu_1(\gamma_1 - (x_1 + \alpha x_3))}, \quad (4)$$

where μ_0 is the baseline apoptosis rate, and μ_1, γ_1 determine the sensitivity of cell death to signal withdrawal.

The formulations (4) and (1) together ensure that cells with low x_1 (due to drug inhibition) and low x_3 (lack of adaptation) undergo high rates of apoptosis, whereas DTPs and DRCs survive through elevated x_2 (quiescence, avoiding μ in proliferative phase) or elevated x_3 .

Impact of drug treatment

The targeted therapy exerts selective pressure by suppressing the growth signal. We model this by reducing the basal capacity θ_0 , which recovers only if cells upregulate the adaptive state x_3 . To describe this dynamic adaptation, we introduce a drug-dependent modulation factor $\eta(x_3)$:

$$\theta_0(\mathbf{x}) = \begin{cases} \bar{\theta}_0, & \text{Control (No drug),} \\ \bar{\theta}_0 \cdot \eta(x_3), & \text{Treatment (With drug),} \end{cases} \quad (5)$$

where the recovery factor $\eta(x_3)$ is governed by a sigmoid function $\psi(x_3)$:

$$\eta(x_3) = 1 - (1 - \eta_0)\psi(x_3), \quad \text{with} \quad \psi(x_3) = \frac{1}{1 + e^{k(x_3 - \bar{x}_3)}}. \quad (6)$$

Biologically, immediately upon drug administration, θ_0 drops to $\eta_0 \bar{\theta}_0$, resulting in the suppression of the cell population. However, as cells evolve toward the DRC phenotype (increasing x_3), $\psi(x_3)$ approaches 0, restoring $\eta(x_3) \approx 1$. This captures the emergence of resistance where cells regain proliferative fitness despite the presence of the drug.

2.1.3 The inheritance probability kernel $p(\mathbf{x}, \mathbf{y})$

To efficiently capture the phenotypic plasticity without resolving detailed intracellular networks, we introduce a phenomenological inheritance probability kernel $p(\mathbf{x}, \mathbf{y})$. This kernel defines the conditional probability density that a mother cell with state \mathbf{y} generates a daughter with state \mathbf{x} , satisfying the normalization condition:

$$\int_{\Omega} p(\mathbf{x}, \mathbf{y}) d\mathbf{x} = 1, \quad \forall \mathbf{y} \in \Omega. \quad (7)$$

Biologically, this kernel aggregates molecular noise (e.g., chromatin remodeling) into a stochastic memory process, balancing high-fidelity inheritance with the epigenetic drift required for evolution. Mathematically, it acts as the integral transition operator in the population dynamics equation (see Appendix A), linking microscopic fluctuation to macroscopic population shifts (Lei 2020b).

Mathematical formulation of the probability kernel

Although the biological traits x_1, x_2 , and x_3 are functionally coupled (e.g., via mutual inhibition pathways), we assume that the stochastic fluctuations affecting each trait during cell division are statistically independent. This simplifies the high-dimensional joint probability distribution into a product of marginal distributions:

$$p(\mathbf{x}, \mathbf{y}) = \prod_{i=1}^3 p_i(x_i, \mathbf{y}),$$

where $p_i(x_i, \mathbf{y})$ is the inheritance function for the i -th component. Crucially, this factorization implies independence only in the noise structure, not in the phenotypes themselves. The biological correlations among traits are rigorously preserved and encoded within the conditional expectation function of these distributions (detailed below), ensuring that the simulated cells exhibit realistic phenotypic coupling.

Since the state variables x_i reflect the expression levels of marker proteins or mRNA, which typically follow right-skewed, non-negative distributions (Friedman et al. 2006; Shahrezaei and Swain 2008), we model $p_i(x_i, \mathbf{y})$ using a Gamma distribution:

$$\begin{aligned} p_i(x_i, \mathbf{y}) &= \text{Gamma}(x_i; a_i(\mathbf{y}), b_i(\mathbf{y})) \\ &= \begin{cases} \frac{b_i(\mathbf{y})^{-a_i(\mathbf{y})}}{\Gamma(a_i(\mathbf{y}))} x_i^{a_i(\mathbf{y})-1} e^{-x_i/b_i(\mathbf{y})}, & x_i \geq 0, \\ 0, & x_i < 0, \end{cases} \end{aligned} \quad (8)$$

where $\Gamma(\cdot)$ is the Gamma function. The parameters $a_i(\mathbf{y})$ (shape) and $b_i(\mathbf{y})$ (scale) depend on the mother cell state \mathbf{y} .

The conditional expectation and variance of x_i are related to the Gamma parameters by

$$\text{E}(x_i|\mathbf{y}) = a_i(\mathbf{y})b_i(\mathbf{y}), \quad \text{Var}(x_i|\mathbf{y}) = a_i(\mathbf{y})b_i^2(\mathbf{y}). \quad (9)$$

Hence,

$$a_i(\mathbf{y}) = \frac{\text{E}(x_i|\mathbf{y})^2}{\text{Var}(x_i|\mathbf{y})}, \quad b_i(\mathbf{y}) = \varphi_i(\mathbf{y})/a_i,$$

where $\varphi_i(\mathbf{y}) = \text{E}(x_i|\mathbf{y})$ denotes the conditional expectation of x_i . In practice, we often treat the dimensionless parameter a_i as a fixed constant, while $b_i(\mathbf{y})$ is determined by $\varphi_i(\mathbf{y})$. Thus, through the predefined a_i and $\varphi_i(\mathbf{y})$, the scale parameter $b_i(\mathbf{y})$ and the inheritance probability $p_i(x_i, \mathbf{y})$ are determined subsequently.

The conditional expectation $\varphi_i(\mathbf{y})$ is crucial for $p_i(x_i, \mathbf{y})$, as it defines the expected epigenetic state of the daughter cell inherited from the mother cell. We construct this function based on three biological considerations:

1. **Epigenetic memory:** High expression levels in the mother cell (y_i) generally bias daughter cells toward high expression (x_i), enforcing a monotonic dependence of $\varphi_i(\mathbf{y})$ on y_i .

2. **Saturation constraints:** Biological transcription and translation rates are physically limited by cellular resources, preventing unbounded accumulation of state variables.
3. **Nonlinear cooperativity:** Epigenetic maintenance often involves cooperative enzyme kinetics (e.g., histone methylation writers effectively recruiting more writers), creating switch-like or sigmoidal responses essential for distinct phenotypic stabilization (Lei 2020b).

Consequently, we model $\varphi_i(\mathbf{y})$ using a generalized Hill function, which naturally captures the transition from linear inheritance memory to saturation:

$$\varphi_i(\mathbf{y}) = \varphi_{i,0}(\mathbf{y}) + \varphi_{i,1}(\mathbf{y}) \frac{y_i^{n_i}}{K_i(\mathbf{y})^{n_i} + y_i^{n_i}}, \quad (10)$$

Here, baseline coefficient $\varphi_{i,0}$ and maximum capacity $\varphi_{i,1}$ determine the bounds of the state variable, while the half-saturation threshold $K_i(\mathbf{y})$ and Hill coefficient n_i determine the sensitivity of the switch. Crucially, by allowing these coefficients to depend on other state components (coupling), we can embed the structure of the underlying gene regulatory network into the inheritance kernel (Li et al. 2025).

Parameter identifiability and drug modulation

The functional form in (10) provides a direct link between model parameters and experimental observables. In a population at dynamic equilibrium, the population-averaged expression level of marker x_i roughly corresponds to the fixed point of the conditional expectation map, governed by the equation $x_i \approx \mathbb{E}[x_i|\mathbf{x}] = \varphi_i(\mathbf{x})$. This relationship allows us to calibrate the coefficients (e.g., $\varphi_{i,0}$, $\varphi_{i,1}$, and K_i) using mean fluorescence intensity (MFI) data from flow cytometry of bulk RNA-seq data.

Furthermore, therapeutic agents do not merely select for pre-existing states but actively remodel the epigenetic landscape. We posit that drug treatment alters the inheritance kernel by modulating the shape coefficients—specifically the baseline coefficients $\varphi_{i,0}$, the maximum capacity $\varphi_{i,1}$, and the sensitivity threshold K_i . This reflects drug-induced transcriptional reprogramming.

In the following, we specify the explicit forms of $\varphi_i(\mathbf{y})$ for each epigenetic state variable x_i . Unless otherwise specified, all parameters are positive constants. The drug concentration is denoted by a normalized variable D , where $0 \leq D \leq 1$.

1. Regulation of drug sensitivity (x_1).

The inheritance of sensitivity markers (e.g., EGFR) is disrupted by drug exposure and modulated by the adaptive state (x_3). We assume:

- **Drug inhibition:** The drug dosage D reduces the expression of x_1 in progeny, reflecting the selection against sensitive phenotypes of drug-induced transcriptional repression.
- **Protective adaptation:** High levels of the adaptive state (x_3) can buffer this drug effect.

These mechanisms are formulated as:

$$\begin{aligned}\varphi_{1,0}(\mathbf{y}) &= \varphi_{10} - Dc_{10}\psi(y_3), \\ \varphi_{1,1}(\mathbf{y}) &= \varphi_{11} - Dc_{11}\psi(y_3), \\ K_1(\mathbf{y}) &= k_{10} + k_{11} \frac{y_3^{n_{K1}}}{(K_{10} - rD)^{n_{K1}} + y_3^{n_{K1}}}.\end{aligned}\tag{11}$$

Here, $\psi(y_3)$ (defined in (6)) corresponds to the drug adaptation that approaches 0 for high y_3 , mitigating the drug-induced domulation ($-Dc\psi(y_3)$). Moreover, the drug increases the saturation threshold K_1 to reduce the expression of x_1 in progeny.

2. Stress-induced stemness (x_2).

Consistent with the concept of adaptability-driven reprogramming (Nie et al. 2022), we assume that drug treatment actively promotes the inheritance of the stem-like state x_2 :

$$\varphi_{2,0}(\mathbf{y}) = \varphi_{20} + Dc_{20}\psi(y_3), \quad \varphi_{2,1}(\mathbf{y}) = \varphi_{21} + Dc_{21}\psi(y_3), \quad K_2(\mathbf{y}) = K_2.\tag{12}$$

Here, the terms $+Dc\psi(y_3)$ imply that under drug pressure (and before full resistance x_3 is acquired), daughter cells tend to have higher stemness, facilitating the transition to DTPs.

3. Adaptation pathway (x_3).

The adaptive state x_3 (e.g., bypass signaling) typically exhibits a see-saw relationship with the primary target x_1 . We model this by making the half-saturation constant K_3 dependent on y_1 :

$$\varphi_{3,0}(\mathbf{y}) = \varphi_{30}, \quad \varphi_{3,1}(\mathbf{y}) = \varphi_{31},\tag{13}$$

with a Hill-type dependence of $K_3(\mathbf{y})$ on y_1 :

$$K_3(\mathbf{y}) = k_{30} + k_{31} \frac{y_1^{n_{K3}}}{K_{30}^{n_{K3}} + y_1^{n_{K3}}}.\tag{14}$$

A high level of y_1 increases $K_3(\mathbf{y})$, which decreases the expectation response $\varphi_3(\mathbf{y})$, effectively suppressing the spontaneous emergence of the resistant state x_3 in sensitive populations.

In summary, while specific parameters are estimated phenomenologically, the structure of $p(\mathbf{x}, \mathbf{y})$ provides a mechanistic hypothesis: drug resistance emerges not just from selection, but from stress-induced biases in the stochastic inheritance of lagile epigenetic states.

2.2 Agent-based stochastic simulation

While the population dynamics of our system are rigorously governed by the IDE derived from stem cell regeneration dynamics (detailed in Appendix A), numerical solution of this equation in a high-dimensional epigenetic space suffers from the curse of dimensionality. To overcome this computational bottleneck and, crucially, to capture

the stochastic extinct events that deterministic models miss, we implement the model using an agent-based stochastic simulation. This approach serves as a Monte Carlo realization of the underlying IDE, where the continuous population density $Q(t, \mathbf{x})$ is approximated by an ensemble of discrete agents.

The computational procedure follows a fixed time-step evolution, outlined in Algorithm 1.

Algorithm 1: Agent-based stochastic simulation

```

1 Initialization: Set time  $t = 0$ , population size  $N = N_0$ , and drug schedule.
  Construct the initial population  $\Sigma = \{C_i(\mathbf{x}, a)\}_{i=1}^N$ . Each cell  $C_i(\mathbf{x}, a)$  is
  characterized by its epigenetic state vector  $\mathbf{x} \in \mathbb{R}_+^3$  and age  $a$ . Initially, all
  cells are synchronized in the resting phase with  $a = 0$ , and therefore the
  resting phase cell number  $Q = N$ .
2 for  $t = 0$  to  $T$  with step  $\Delta t$  do
3   for each cell  $C_i$  in  $\Sigma$  do
4     /* 1. Update kinetic rates based on current state  $\mathbf{x}$  */  

5     Calculate  $\beta(\mathbf{x}, Q)$ ,  $\kappa(\mathbf{x})$ , and  $\mu(\mathbf{x})$ .
6     /* 2. Determine cell fate within the time interval
7        $(t, t + \Delta t)$  (Bernoulli trials) */  

8     Generate a random number  $r \sim \text{Uniform}(0, 1)$ .
9     if cell is in the resting phase then
10      if  $r < \beta\Delta t$  then
11        Transition to proliferation phase; set age  $a = 0$ . State unchanged.
12      else if  $r < (\beta + \kappa)\Delta t$  then
13        Cell undergoes terminal differentiation (removed from  $\Sigma$ ).
14      else if cell is in the proliferation phase then
15        if  $a_i < \tau$  then
16          if  $r < \mu\Delta t$  then
17            Cell undergoes apoptosis (removed from  $\Sigma$ ).
18          else
19            Update age:  $a \leftarrow a + \Delta t$ .
20        else if  $a \geq \tau$  then
21          /* 3. Mitosis and inheritance */  

22          Cell divides into two daughter cells. For each daughter, sample
23          new state  $\mathbf{x}_{\text{new}}$  from the kernel  $p(\mathbf{x}_{\text{new}}, \mathbf{x})$  (Eq. (8)). Reset
24          ages to 0; add daughters to  $\Sigma$  as resting phase cells.
25
26   Update: Update the total population count  $N(t)$  and the resting phase
27   cells  $Q(t)$ ; record system state; advance  $t \leftarrow t + \Delta t$ .

```

The simulation discretizes time into small intervals Δt (set to ensure that transition probabilities $\ll 1$). At each step, cell fate decisions (differentiation, division, apoptosis) are determined via Bernoulli trials comparing the calculated probabilities (e.g.,

$\beta\Delta t, \kappa\Delta t, \mu\Delta t)$ against uniform random numbers. A critical step occurs at mitosis: when a cell divides, the epigenetic states of the two daughter cells are independently sampled from the multivariate Gamma distribution defined by the inheritance kernel $p(\mathbf{x}, \mathbf{y})$. This step introduces the necessary epigenetic noise that fuels phenotypic evolution.

Since the stochastic process converges to the deterministic mean-field limit as the system size $Q \rightarrow \infty$ (a theoretical consistency we validate in Appendix B), our simulation strategy depends on the population scale:

1. Deterministic limit: For simulations in Section 3.1 and 3.2, stochastic fluctuations are negligible relative to the mean trend. Thus, single representative runs are sufficient to characterize the population dynamics.
2. Stochastic regime: For scenarios involving tumor extinction or the initial emergence of rare resistant clones (Fig. 10 and Section 3.4), stochastic effects differ significantly between runs. In these cases, we perform ensembles of independent simulations ($n = 3$ for illustrative traces, $n = 10$ for robustness analysis) to capture the variance and survival probabilities.

2.3 Model Parameterization and Calibration

Parameterizing a high-dimensional agent-based model requires balancing biological plausibility with quantitative accuracy. To ensure the model faithfully reproduces tumor evolutionary dynamics without overfitting, we employed a hierarchical estimation strategy combining literature-derived biological constraints with data-driven calibration.

First, for the fundamental cellular kinetic parameters that govern cell fate decisions—specifically the maximum proliferation rate $\bar{\beta}$, terminal differentiation rate κ_0 , and apoptosis rate μ_0 —we restricted our search space to biologically plausible ranges reported in prior quantitative oncology studies (Lima et al. 2021; Jagiella et al. 2016; McClatchy et al. 2020; Kolokotroni et al. 2016). These physiological constraints (summarized in the Range column of Table 3) ensure that the simulated cellular turnover rates remain consistent with known cell cycle biological limits.

For the phenomenological parameters governing the epigenetic inheritance kernel and drug interactions (e.g., shape parameters and Hill coefficients), we performed a sequential calibration using longitudinal data from osimertinib PC9 xenograft models (Nie et al. 2022). In Nie et al. (2022), PC9 xenograft mice were treated with the EGFR-TKI osimertinib for 9 consecutive days to establish osimertinib-regressed minimal residual disease (MRD) tumors. The drug was then withdrawn for 14 days, resulting in regrown tumors. As illustrated in Fig. 4, the calibration proceeded in three stages:

1. **Baseline Growth ($D = 0$)**: We first disabled the drug term and turned the intrinsic growth parameters to match the tumor volume evolution of the control group (Fig. 4A, black triangles).
2. **Therapeutic Response ($D = 1$)**: Fixing the baseline growth parameters, we then introduced the drug effect to calibrate the sensitivity parameters $(c_{i,j}, r)$, fitting the rapid regression and subsequent regrowth phases observed in the experimental group (Fig. 4A, colored markers).

3. Phenotypic Distributions: To validate the microscopic realism of the model, we fine-tuned the inheritance kernel parameters so that the simulated proportions of sensitive (x_1), stem-like (x_2), and resistant (x_3) cells matched the transcriptomic signatures of control, MRD, and regrown tumors reported in [Nie et al. \(2022\)](#) (Fig. 4B).

To critically evaluate the influence of parameter uncertainty, we conducted a systematic local sensitivity analysis (detailed in Section 3.5.1). This analysis identified that tumor recurrence dynamics are primarily driven by kinetic rates and competition coefficients, while being less sensitive to minor variations in specific kernel shape parameters. Consequently, less sensitive parameters were fixed at their calibrated baseline values to maintain model identifiability, while key sensitive parameters were later varied to construct virtual patients for exploring treatment heterogeneity.

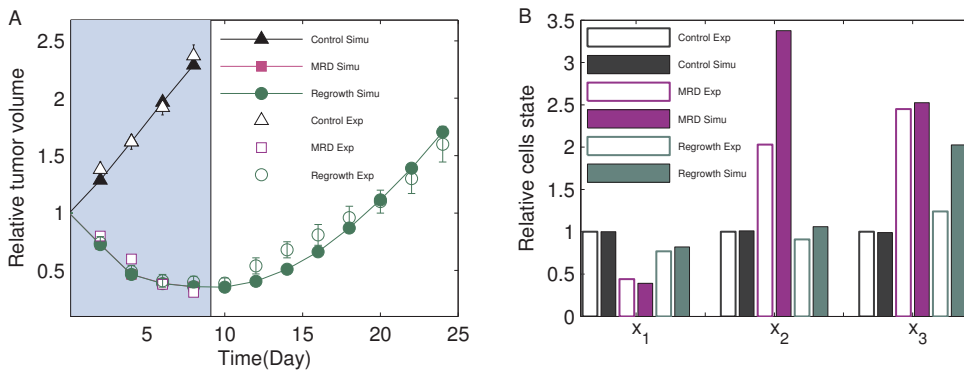


Fig. 4 Model calibration against in vivo data. **A** Fitting of macroscopic tumor volume dynamics. The model (solid lines) accurately captures both the unperturbed growth of Control tumors ($D = 0$) and the regression-relapse trajectory of osimertinib-treated tumors ($D = 1$). Experimental data (symbols, mean \pm SEM) derived from PC9 xenografts in [Nie et al. \(2022\)](#). **B** Validation of microscopic phenotypic heterogeneity. The simulated proportions of microscopic phenotypic heterogeneity. The simulated proportions of epigenetic states correspond to the relative expression levels observed in distinct tumor phases (Control, MRD, Regrowth), confirming the model's ability to reproduce drug-induced phenotypic plasticity. Experimental benchmarks derived from [Nie et al. \(2022\)](#) and [Aissa et al. \(2021\)](#).

A complete summary of the baseline parameter values, their units, and the sources of their derivations is provided in Table 3. Unless otherwise specified in the figure legends, all subsequent simulations typically utilize these baseline parameter values.

Table 3 Summary of key system parameters used in the simulations.

Parameter	Description	Value	Unit	Source/Method
$\bar{\beta}$	Maximum proliferation rate	0.118*	h^{-1}	Range 0.01–0.4 (1-4)
$\bar{\theta}_0$	Proliferation saturation capacity	5.9×10^2	cells	Cali. Control
m	Hill coefficient (proliferation)	1	-	Assumed (Standard)
η_0	Drug effect on $\bar{\theta}_0$	0.66	-	Cali. Treated
κ_0	Maximum differentiation rate	0.051*	h^{-1}	Range 10^{-4} – 10^{-1} (1-4)
τ	Proliferative phase duration	18	h	Range 12–36 (1-4)
μ_0	Maximum apoptosis rate	0.0071*	h^{-1}	Range 10^{-4} – 10^{-1} (1-4)
μ_1	Effective coefficient of x_1 and x_3 to apoptosis	0.65	h^{-1}	Cali. Treated
α	Relative weight of x_3 of joint effect	0.95*	-	Estimated
\bar{x}_3	Adaption threshold of x_3	4.2	-	Cali. Phenotype
γ_1	Baseline combined effect of x_1 and x_3	5.5	-	Estimated
φ_{10}	Hill coefficient for x_1	0.7	-	Cali. Phenotype
φ_{11}	Hill coefficient for x_1	4.9	-	Cali. Phenotype
c_{10}	Drug effect coefficient on x_1	0.18	-	Cali. Treated
c_{11}	Drug effect coefficient on x_1	2.45	-	Cali. Treated
k_{10}	Effect of x_3 on x_1	0.7	-	Cali. Treated
k_{11}	Effect of x_3 on x_1	3.45	-	Cali. Treated
φ_{20}	Hill coefficient for x_2	0.65	-	Cali. Phenotype
φ_{21}	Hill coefficient for x_2	4.5	-	Cali. Phenotype
c_{20}	Drug effect coefficient on x_2	0.2	-	Cali. Treated
c_{21}	Drug effect coefficient on x_2	2.0	-	Cali. Treated
K_{10}	Half-effective coefficient of K_1	2.6	-	Estimated
K_2	Half-effective coefficient of x_2	3.45	-	Estimated
K_{30}	Half-effective coefficient of K_3	2.3	-	Estimated
r	Drug effect coefficient on K_{10}	0.3	-	Cali. Treated
φ_{30}	Hill coefficient for x_3	0.7	-	Cali. Phenotype
φ_{31}	Hill coefficient for x_3	4.9	-	Cali. Phenotype
k_{30}	Effective coefficient of x_1 to x_3	0.7	-	Estimated
k_{31}	Effective coefficient of x_1 to x_3	3.45	-	Estimated
n_i	Hill coefficient for x_i ($i = 1, 2, 3$)	2	-	Estimated
n_{K_i}	Hill coefficient for x_i ($i = 1, 3$)	4	-	Estimated
a	Shape parameter of Gamma distribution	50	-	Range 30–120 (5)
a_1	Coefficient in (1)	1.3	-	Cali. Control
a_2	Coefficient in (1)	0.33	-	Cali. Control
a_3	Coefficient in (1)	0.75	-	Cali. Control
a_4	Coefficient in (1)	0.23	-	Cali. Control
a_5	Coefficient in (1)	10.0	-	Cali. Control
κ_1	Coefficient in (2)	0.6	-	Cali. Control
k	Coefficient in (6)	5	-	Cali. Treated

Methods: “Range” indicates values constrained by literature-constrained biological priors; “Cali.” indicates values calibrated by fitting simulation results to data in Fig. 4 (Control, Treated, or Phenotype heterogeneity); “Estimated” indicates parameters with low sensitivity and estimated based on biological priors.

Sources: 1=Lima et al. (2021), 2=Jagiella et al. (2016), 3= McClatchy et al. (2020), 4=Kolokotroni et al. (2016), 5=Lei (2020b).

*: Parameters with high sensitivity and are varied to generate virtual patient cohorts.

3 Results

3.1 Tumor evolution dynamics in the absence of treatment

We first investigated the intrinsic tumor evolution dynamics in the absence of drug administration ($D(t) = 0$). To examine tumor cell plasticity during tumor expansion, we initialized the system with a naive population of 4×10^3 cells, assigning initial epigenetic states x_i uniformly distributed on $[0, 8]$. The parameter α governs the competition between the complementary pathways associated with drug-sensitive (x_1) and resistant (x_3). We analyzed two distinct scenarios, $\alpha = 0.95$ and $\alpha = 1.0$, tracking both the macroscopic population growth and microscopic phenotypic drift (Fig. 5).

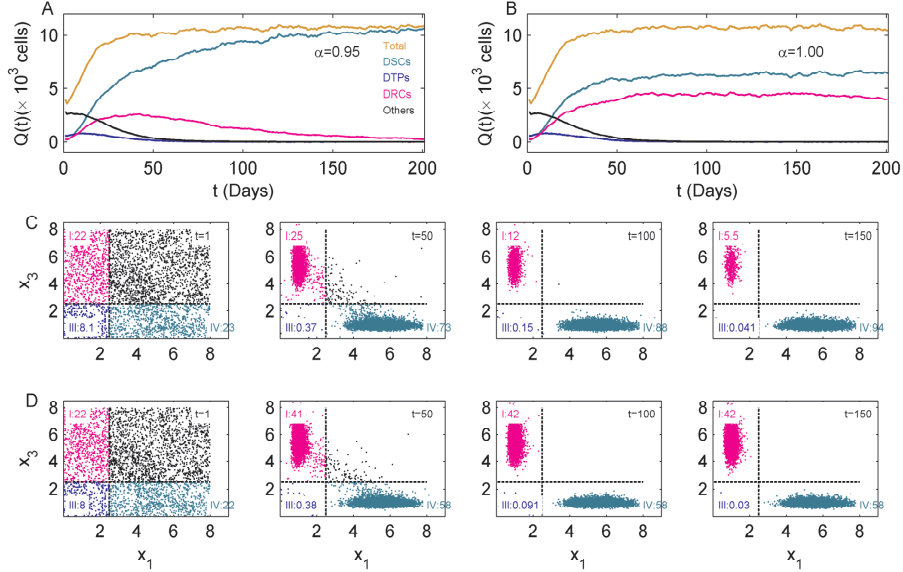


Fig. 5 Intrinsic tumor evolution driven by different competition parameter α . **A** and **B** Temporal evolution of tumor subpopulations starting from a uniform epigenetic state distribution, with **A** biased competition ($\alpha = 0.95$), and **B** balanced competition ($\alpha = 1.0$). Subpopulations are color-coded: Total tumor cells (orange), DSCs (pale teal), DTPs (blue), DRCs (magenta), and other phenotypes (black). **C** and **D** Evolution of the epigenetic landscape (x_1, x_3) at days 1, 50, 100, and 150, with **C** $\alpha = 0.95$, and **D** $\alpha = 1.0$. Black dashed lines indicate the phenotypic threshold (see Table 2), partitioning the state space into four distinct quadrants: I(Non-viable/Others, black), II(DRCs, magenta), III(DTPs, blue), IV(DSCs, pale teal). Percentages denote the cell fraction within each quadrant.

For the cast of $\alpha = 0.95$, the total tumor burden increased rapidly before reaching saturation around day 50 (Fig. 5A). Interestingly, while the macroscopic volume stabilized, the internal population structure continued to evolve. The fraction of drug-resistant cells (DRCs) spontaneously declined from 20% to 5.5%, while drug-sensitive cells (DSCs) expanded from 73% to 94% between days 50 to 150 (Fig. 5C). This indicates that in a drug-free environment, the system exhibits a natural selection pressure favoring the highly proliferative sensitive phenotype.

In contrast, when $\alpha = 1.0$, representing an equal fitness potential for adaptive pathways, the macroscopic growth trajectory remained similar, but the steady-state composition differed markedly (Fig. 5B). The population settled into a heterogeneous equilibrium with substantial proportions of both DRCs ($\sim 42\%$) and DSCs ($\sim 58\%$) (Fig. 5D). These results demonstrate that the competition coefficient α is a critical determinant of the intrinsic heterogeneity level within the tumor.

Since clinically observable EGFR-mutant tumors are typically dominated by drug-sensitive clones prior to TKI treatment (reflecting the fitness cost often associated with resistance mechanisms absent drug pressure), we selected $\alpha = 0.95$ for the subsequent simulations to replicate this clinically relevant baseline.

3.2 Dynamics of DTPs-mediated drug resistance

To investigate how drug-tolerant persister (DTP) cells drive drug resistance, we simulated the evolution of epigenetic states under short-term EGFR-TKI treatment calibrated to PC9 xenograft mice (Nie et al. 2022). Experimental observations show that tumor volume markedly decreases during drug treatment (days 1–9), but relapses after drug withdrawal, eventually exceeding 150% of its pre-treatment size by day 24 (Fig. 4A).

Figure 6 depicts the evolution of drug sensitivity (x_1) and adaptation (x_3) states during treatment and tumor relapse. During remission (days 1–9), DSCs with high x_1 were depleted, while DTPs with elevated x_3 emerged. Between days 10 and 14, following drug withdrawal, both drug-sensitive and drug-tolerant populations expanded, whereas the fraction of transition cells (with simultaneously low x_1 and x_3) declined. By day 14, a stable drug-resistant phenotype characterized by high x_3 and low x_1 was established. At later stages (days 20–24), cells segregated into distinct phenotypic clusters with well-separated x_1 and x_3 states. Notably, by day 24, about 62% of cells had reverted to a drug-sensitive state, indicating that a substantial fraction of the population can re-establish sensitivity once treatment is discontinued.

To further characterize tumor cell plasticity and heterogeneity during relapse, we analyzed the evolution of phenotypic fractions (Fig. 7). Phenotypes were defined according to Table 2. Prior to treatment (day 0), the majority of cells were DSCs, characterized by high x_1 and low x_2, x_3 . During treatment, the DSC fraction dropped sharply, and surviving cells transitioned into DTPs (day 9), showing upregulated x_2 and x_3 along with reduced x_1 . At this time, many cells displayed mixed features corresponding to intermediate transitional states. After treatment withdrawal, the DSC fraction progressively increased as x_1 was restored. DTPs largely disappeared by day 24, whereas DRCs rose to 36%. Prolonged simulation predicted that the DRC fraction would eventually decline to zero by day 150 (Fig. 9A). Together, these results highlight the molecular state transitions underlying DTP-induced resistance and demonstrate that our model captures experimentally observed tumor relapse dynamics.

We next examined how cell plasticity influences relapse dynamics by varying the shape parameter a in the inheritance function $p(\mathbf{x}, \mathbf{y})$. The parameter a associates with the shape parameter of the Gamma distribution (8). A larger a corresponds to a narrow distribution (less variance) for fixed means, and increasing a effectively reduces the stochastic phenotypic drift (plasticity) during cell division.

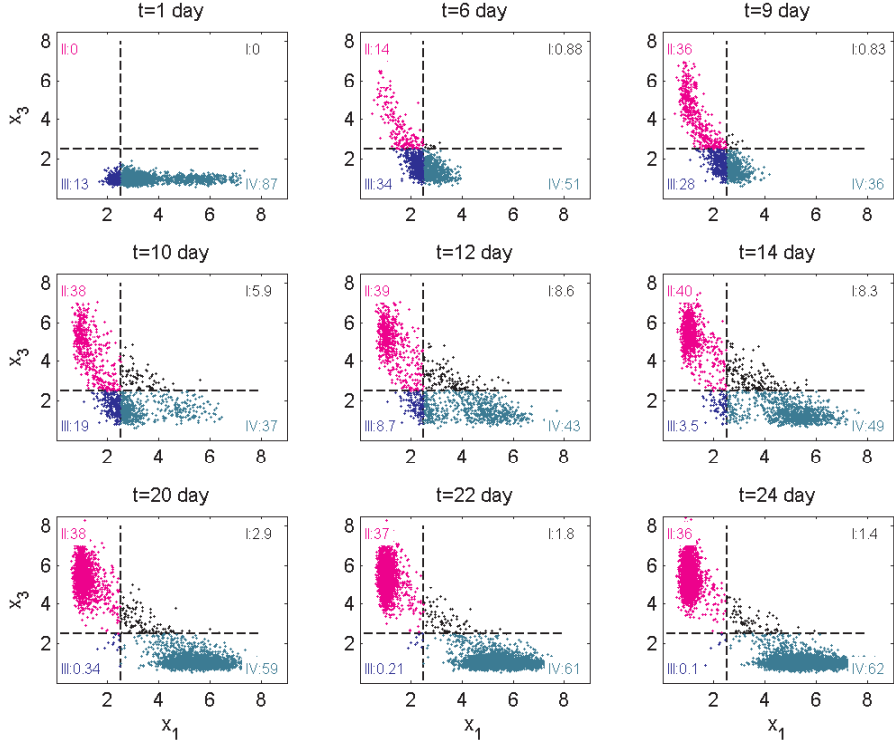


Fig. 6 Evolution of epigenetic states (x_1, x_3) following drug treatment. Each point corresponds to an individual tumor cell in the (x_1, x_3) plane. The plane is partitioned into four quadrants defined by the phenotype threshold in Table 2, with colors indicating the respective regions. The percentage values denote the fraction of cells residing in each quadrant. Parameter settings are identical to those used in Fig. 4.

Simulations with $a = 25$ and $a = 75$ revealed that higher a accelerated tumor relapse (Fig. 8A). Analyzing DSC and DRC populations separately showed that a larger a yielded a smaller DRC fraction and a larger DSC fraction (Fig. 8B). These results suggest that reduced plasticity diminishes the generation of DRCs and favors the faithful restoration of DSCs. Because sensitive cells proliferate naturally faster than resistant ones, higher inheritance fidelity (reduced plasticity) ultimately accelerates regrowth, leading to a higher tumor burden after treatment withdrawal.

These simulations demonstrate that DTPs act as a transient reservoir enabling tumor survival during treatment and shaping relapse dynamics through their interplay with both drug-sensitive and drug-resistant populations.

3.3 Formation of irreversible drug-resistant cells

Experimental studies have demonstrated that DTPs are transient and reversible: they can survive short-term drug exposure but typically revert to a drug-sensitive phenotype once treatment is withdrawn (Sharma et al. 2010). However, prolonged drug administration may drive a transition from DTPs to irreversible DRCs. Unlike DTPs,

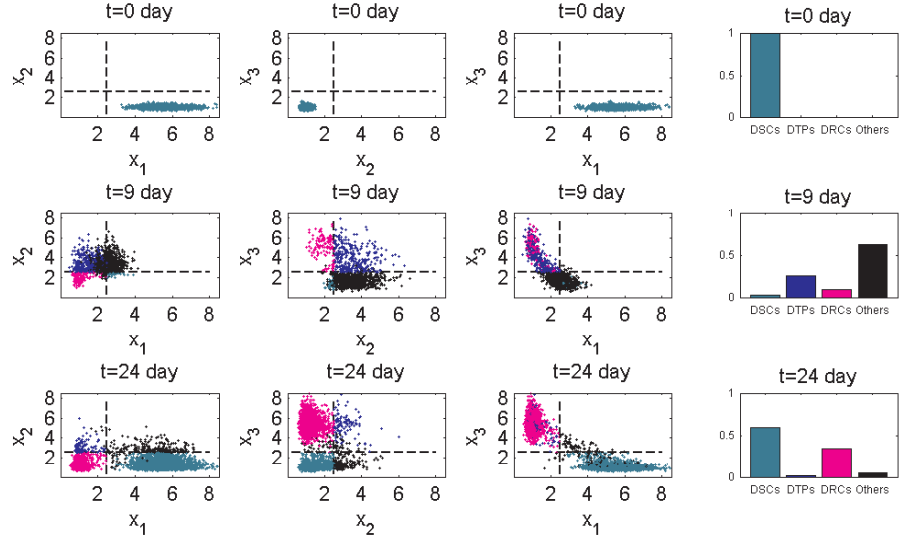


Fig. 7 Epigenetic state dynamics during tumor regrowth. Scatter plots show the distributions of (x_1, x_2) , (x_2, x_3) , and (x_3, x_1) at days 0, 9, and 24 after treatment. Each point represents an individual tumor cell. Colors denote cell phenotypes: DSCs (pale teal), DTPs (blue), DRCs (magenta), and other phenotypes (black). Black dashed lines mark the threshold values x_s^i that define phenotype boundaries (see Table 2). The rightmost column summarizes the phenotype proportions at each time point.

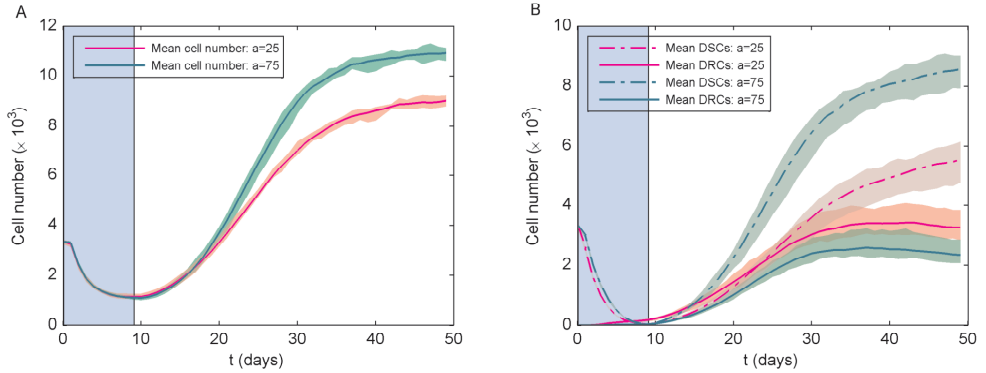


Fig. 8 Relapse dynamics under different plasticity parameters **A.** Simulations followed the same protocol as in Fig. 4, with continuous drug treatment applied for 9 days. Model parameters are given in Table 3. For each a , ten independent simulations with different random seeds were performed; solid lines represent mean trajectories, and shaded regions indicate the range across replicates. **A** Total tumor cell numbers for $a = 25$ (magenta) and $a = 75$ (pale teal). **B** Dynamics of DSC and DRC subpopulations for $a = 25$ (magenta) and $a = 75$ (pale teal). Solid lines correspond to DSCs, and dash-dotted lines to DRCs. Increased plasticity ($a = 75$) accelerates the expansion of DRCs and promotes earlier relapse compared to low plasticity $a = 25$. Lines represent the mean of 3 independent simulations, and the shaded regions indicate the Mix-to-Max range.

DRCs maintain resistance even after drug withdrawal and recover proliferative capacity comparable to the original DSCs (Marine et al. 2020). Here, we utilized our model to investigate the emergence of irreversible resistance and tumor progression under prolonged drug treatment.

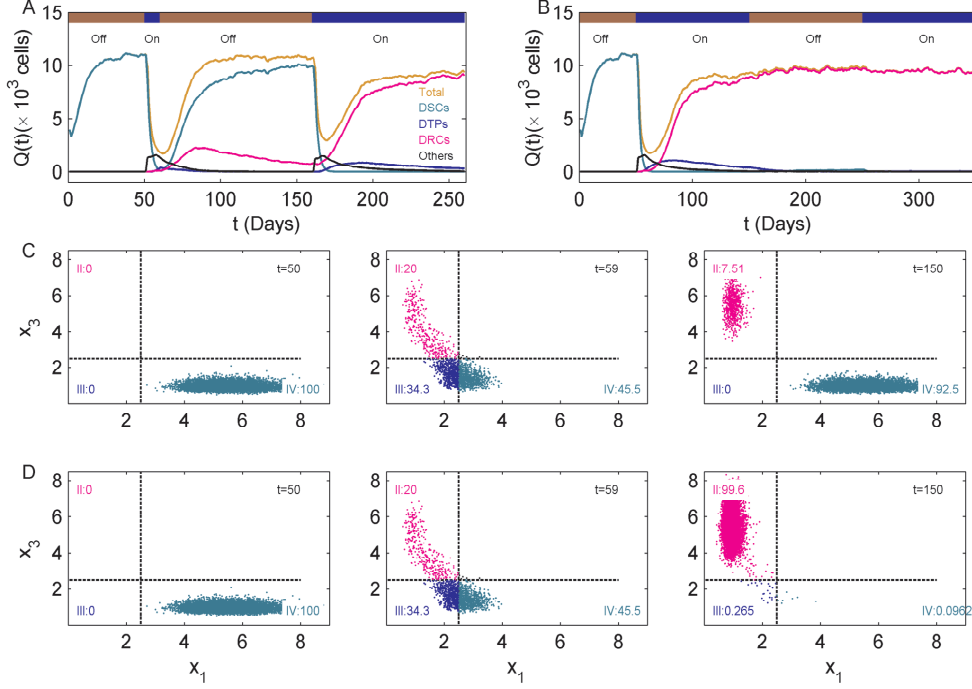


Fig. 9 Tumor evolution under short- and long-term drug treatments. **A** Cell number dynamics and **C** epigenetic states (x_1, x_3) at different time points following short-term treatment. **B** Cell number dynamics and **D** epigenetic states (x_1, x_3) at different time points following long-term treatment. All tumors were initialized with DSCs. In A and C, the drug was applied during $50 \leq t \leq 60$ and $160 \leq t \leq 260$. In B and D, the drug was applied during $50 \leq t \leq 150$ and $250 \leq t \leq 350$. In C and D, the four quadrants of $(x_1, x_3) \in [0, 8] \times [0, 8]$ are color-coded: I(black), II(magenta), III(blue), IV(pale teal). Numbers indicate the proportions of cells in each quadrant. Short-term treatment suppresses growth transiently without altering epigenetic diversity, whereas long-term treatment profoundly shifts cell states and promotes resistant subpopulations.

To compare tumor responses to short- and long-term treatment, we simulated two protocols: (i) a short 10-day treatment followed by a 100-day drug-free period before retreatment, and (ii) a long 100-day treatment followed by the same drug-free period and retreatment (Fig. 9).

During the short-term treatment, tumor cell numbers declined sharply upon drug administration, accompanied by a transient rise in DTPs and DRCs (Fig. 9A). In the epigenetic state space, DSCs with high x_1 shifted toward regions of reduced x_1 and elevated x_3 , indicating a rapid transition into DTPs and DRCs (middle panel of

Fig. 9C). After drug withdrawal, DSCs expanded and gradually regained dominance, while DRCs persisted at low levels due to competitive suppression by faster-growing DSCs. By day 160, approximately 93% of cells had restored their drug-sensitive state (right panel of Fig. 9C). Upon retreatment, most cells were again eliminated, though the tumor nadir (minimum) was higher than during the first treatment cycle due to the residual resistant subpopulation. Nevertheless, these dynamics are consistent with experimental observations that DTPs are reversible under short-term therapy (Sharma et al. 2010; Ramirez et al. 2016).

In contrast, under long-term continuous treatment (Fig. 9B), DRCs progressively adapted to the drug environment and became the dominant population by day 150, while DSCs declined to negligible levels. DTPs initially increased during the first 20 days of treatment but subsequently decreased, indicating a continuous flux from transient tolerance to stable resistance. The corresponding changes in x_1 and x_3 reveal a clear phenotypic inversion, with most cells adopting a drug-resistant phenotype by day 150 (right panel of Fig. 9D). After drug withdrawal, DRCs remained the predominant population, and retreatment at day 250 elicited little response, confirming the establishment of irreversible resistance.

The above simulations demonstrate that our model recapitulates the experimentally observed distinction between short-term reversible tolerance and long-term irreversible resistance, and identifies the DTP-to-DRC transition as a key mechanism driving stable therapeutic failure.

3.4 Dynamic therapies

Continuous treatment promotes the emergence of irreversible DRCs and tumor recurrence, whereas short-term treatment tends to generate reversible DTPs. To restore drug sensitivity and delay resistance, dynamic treatment strategies involving drug discontinuation (“drug holidays”) have been proposed. Two widely studied approaches are intermittent therapy and adaptive therapy. In both cases, the timing of drug administration and withdrawal is critical for therapeutic efficacy. We used our model to simulate and compare the effects of these strategies.

3.4.1 Intermittent therapy

Intermittent therapy applies drugs in periodic on/off cycles. In our simulations, treatment was initiated at day 50, with the drug administered for T_{on} days followed by a drug-free interval of T_{off} days. Each $(T_{\text{on}}, T_{\text{off}})$ combination defines a therapy protocol. The cycle was repeated until tumor recurrence, defined as the tumor size exceeding 8×10^3 cells. We quantify treatment efficacy using the tumor relapse time, defined as the duration from the start of treatment to recurrence:

$$\text{tumor relapse time} = \min_{t>50} \{t | N(t) > 8000\} - 50. \quad (15)$$

We tested various $(T_{\text{on}}, T_{\text{off}})$ combinations, performing 10 independent simulations per case. The average relapse times are summarized in Fig. 10A. Results indicate that proper coordination of drug exposure and holidays is essential to maximize relapse

time. The longest delay (94 days) occurred with $(T_{\text{on}}, T_{\text{off}}) = (2, 6)$, whereas poorly timed drug holidays (e.g., $T_{\text{off}} \geq 10$) led to rapid relapse within 10 days. Increasing T_{on} beyond 20 days provided no further benefit, with relapse times plateauing near 45 days regardless of T_{off} .

To assess robustness, we compared relapse times across independent runs (Fig. 10B). Most combinations yielded consistent outcomes, except for $(T_{\text{on}}, T_{\text{off}}) = (2, 8)$, where some runs resulted in early relapse (10 days) and others in late relapse (90 days). This variability suggests that for certain protocols, outcomes are highly sensitive to intrinsic stochastic in tumor evolution, leading to unpredictable responses.

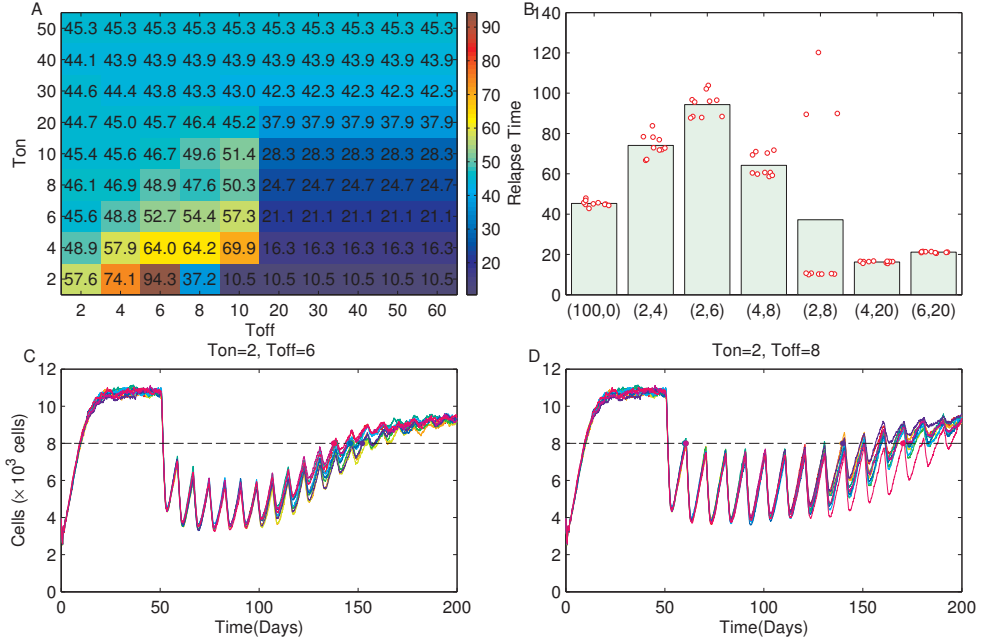


Fig. 10 Tumor relapse time under intermittent therapy. **A** Heatmap of tumor relapse time across different combinations of T_{on} (duration of drug on) and T_{off} (duration of drug off). **B** Tumor relapse time from independent simulation runs for different $(T_{\text{on}}, T_{\text{off}})$ combinations. Bars represent the average relapse time, while circles denote the relapse time from 10 independent runs. The first column (100, 0) corresponds to continuous treatment, and subsequent columns represent intermittent therapy with specified $(T_{\text{on}}, T_{\text{off}})$. **C** and **D** Tumor dynamics for 10 independent runs for selected $(T_{\text{on}}, T_{\text{off}})$ combinations. Each curve shows tumor cell number over time. Black dotted lines indicate the relapse threshold, and filled circles mark the time points when tumors cross this threshold. Intermittent therapy prolongs relapse time compared to continuous treatment, but the outcome strongly depends on the choice of T_{on} and T_{off} .

We next examined tumor dynamics under selected schedules (Fig. 10C–D). With short T_{on} , tumor burden declined during treatment but rebounded during holidays. When subsequent treatments were applied before the tumor reached the relapse threshold, long-term control was achievable (Fig. 10C). However, prolonged drug-free

intervals allowed tumors to cross the threshold prematurely, shortening relapse time (Fig. 10D). These results highlight that fixed-interval schedules may not be optimal, emphasizing the critical importance of treatment timing.

3.4.2 Adaptive therapy

Adaptive therapy dynamically adjusts treatment according to tumor burden (Gatenby et al. 2009). The rationale is to maintain a stable tumor size by preserving a population of drug-sensitive cells that competitively suppress resistant subpopulations. In our simulations, therapy was turned on when tumor size exceeded a threshold P_{on} and turned off when it dropped below a lower threshold P_{off} (with $P_{\text{on}} \geq P_{\text{off}}$).

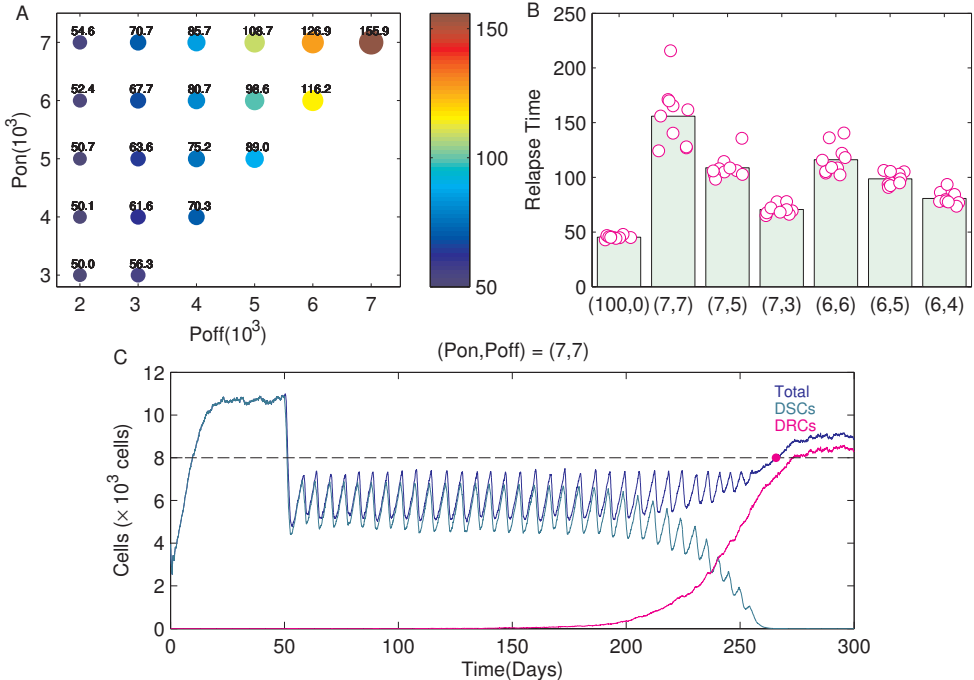


Fig. 11 Tumor relapse time under adaptive therapy. **A** Heatmap of relapse time across different combinations of drug on/off thresholds. P_{on} and P_{off} denote the thresholds for drug initiation and withdrawal, respectively. **B** Comparison of continuous treatment with adaptive therapy. The first column shows the results of continuous treatment, while subsequent columns represent adaptive therapy at specified $(P_{\text{on}}, P_{\text{off}})$ values. Bars indicate the average relapse time, and magenta circles correspond to individual stochastic simulation runs. **C** Tumor evolution dynamics under adaptive therapy with $(P_{\text{on}}, P_{\text{off}}) = (7, 7)$. Curves represent the trajectories of total tumor cells (blue), DSCs (pale teal), and DRCs (magenta). The black dotted line marks the relapse threshold, and the magenta dot indicates the time point when the tumor crosses this threshold. Adaptive therapy prolongs relapse compared to continuous treatment, with outcomes depending on the choice of threshold values.

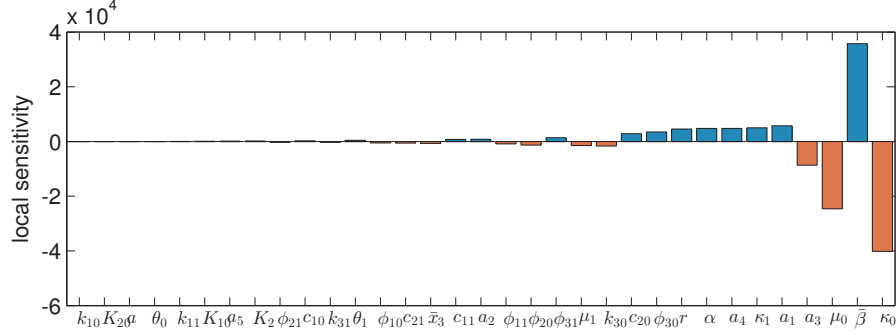


Fig. 12 Local sensitivity analysis (LSA) for parameter selection. Sensitivity of tumor relapse time (R_t) to model parameters under a treatment window of $t \in [50, 150]$. Parameters are ranked by the absolute magnitude of their sensitivity. Light blue bars indicate a positive correlation (increasing the parameter delays relapse), while bright orange bars indicate a negative correlation.

Fig. 11A shows the average relapse times for different $(P_{\text{on}}, P_{\text{off}})$ strategies, based on 10 independent simulations per case. Adaptive therapy markedly extended relapse times compared with intermittent therapy. Increasing either threshold generally postponed relapse. Moreover, results across runs were highly consistent (Fig. 11B), indicating robust therapeutic outcomes. By contrast, continuous therapy yielded an average relapse time of only 50 days, underscoring the advantage of adaptive control.

To illustrate the dynamics, Fig. 11C shows tumor composition for $(P_{\text{on}}, P_{\text{off}}) = (7, 7)$. Here, DRCs remained consistently suppressed by DSCs throughout repeated ON/OFF cycles. Unlike long continuous therapy, which drives rapid DRC expansion (cf. Fig. 9B), adaptive therapy maintained DRCs at low levels until their eventual takeover triggered relapse.

3.5 Virtual clinical trials and patient stratification

3.5.1 Generation and validation of the virtual patient cohort

In-silico clinical trials using virtual patients (VPs) provide a powerful framework to assess the therapeutic strategies in the presence of interpatient heterogeneity. Here, a virtual patient is defined as a specific instance of the mathematical model, characterized by a unique vector of physiological parameters sampled from biological distributions. This approach allows us to explore how individual variations in model parameters influence treatment outcomes without the logistical constraints of physical trials.

To construct a representative VP cohort, we first identified the most critical parameters driving treatment response via local sensitivity analysis (LSA). We examined the sensitivity of the relapse time R_t (defined as the first time the tumor burden exceeds 8,000 cells) to small perturbations in the definition parameters list in Table 3, under a standard treatment window $t \in [50, 150]$. The local sensitivity index for the i -th parameter θ_i is calculated as:

$$LSA_i = \frac{\partial R_t}{\partial \theta_i}.$$

As shown in Fig. 12, parameters governing cellular kinetics—specifically the proliferation rate $\bar{\beta}$, maximum differentiation rate κ_0 , and basal apoptosis rate μ_0 —exhibit the highest impact on relapse time. Additionally, the competition coefficient α , which indicates the fitness cost of resistance, was included due to its direct role in shaping the evolutionary landscape. Consequently, each virtual patient is represented by a parameter vector $(\bar{\beta}, \kappa_0, \alpha, \mu_0)$, while other less sensitive parameters were held constant.

The virtual cohort was generated using a Gaussian Mixture Model (GMM) to capture the realistic distribution of these four parameters (see Appendix C for sampling details). To validate the physiological relevance of our cohort, we compared the simulated progression-free survival (PFS) under continuous therapy against clinical data from the EURTAC trial, a pivotal Phase 3 study comparing erlotinib with chemotherapy in EGFR-mutant NSCLC (Rosell et al. 2012). Our model accurately reproduced the clinical Kaplan-Meier curves (Figure 13A, blue vs. pale teal), confirming that the generated virtual population captures the essential heterogeneity observed in real-world patients.

3.5.2 Mechanisms determining therapeutic benefit

We next evaluated the efficacy of adaptive therapy $(P_{\text{on}}, P_{\text{off}}) = (7, 7)$ within this validated cohort. While the overall population showed a clear survival benefit compared to continuous treatment (Fig. 13A, magenta line), the degree of benefit varied significantly across individuals. To quantify this, we defined the Relapse Time Gain (RTGain) for each patient as:

$$\text{RTGain} = T_{\text{relapse}}^{\text{adaptive}} - T_{\text{relapse}}^{\text{continuous}}. \quad (16)$$

By projecting RTGain onto the parameter space (Fig. 13B-G), we identified three distinct mechanistic zones that explain why some patients benefit from adaptive therapy while others do not:

1. High Proliferation Zeon (Negative Gain): Patients with high proliferation rates $(\bar{\beta}) > 0.07$, Fig. 13B) exhibited negative RTgain. In these highly aggressive tumors, the rapid regrowth during drug holidays outpaces the suppression exerted by sensitive cells. Consequently, the tumor rebounds prematurely before the next treatment cycle can be effective. For such patients, continuous maximum-tolerated dose (MTD) therapy remains the superior strategy.
2. Ecological Control Zone (High Gain): The most significant benefits (RTGain > 0) were observed in patients with low proliferation rates $(\bar{\beta} < 0.02$, Fig. 13B), particularly when combined with high intrinsic apoptosis ($\mu_0 > 1.2 \times 10^{-3}$) and lower resistant fitness ($\alpha < 0.95$) (Fig. 13F-G). In this regime, the slower growth and higher turnover of the tumor allow for effective ecological control. During drug holidays, the restored drug-sensitive population effectively outcompetes resistant clones, suppressing their expansion and prolonging the time to resistance.
3. Intermediate Compensation Zone: In the transition region where proliferation is moderate, positive outcomes are still achievable through a compensatory mechanism. Even if $\bar{\beta}$ is relatively high, a combination of stronger apoptosis pressure

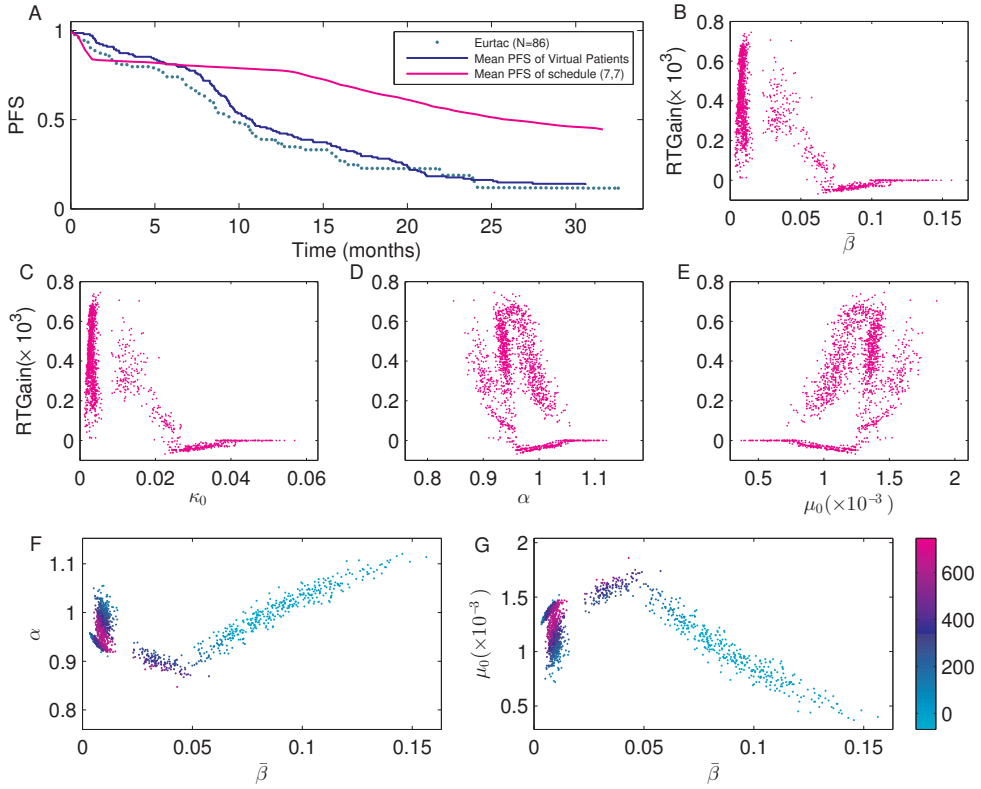


Fig. 13 Stratification of therapeutic outcomes in virtual patients. **A** Progression-free survival (PFS) Kaplan-Meier curves. The virtual cohort (blue line) reproduces the clinical EURTAC trial data (pale teal dotted line) under continuous therapy. Adaptive therapy (magenta line) significantly extends overall PFS. **B–E** Dependencies of Relapse Time Gain (RTGain) on the four key parameters across the cohort. **F–G** Two-dimensional stratification of patient response. Scatter plots showing RTGain (color-coded) as a function of proliferation rate $\bar{\beta}$ vs. competition α (F) and apoptosis μ_0 (G). Three distinct zones (High Proliferation/Failure, Ecological Control/Success, and Intermediate) reveal the mechanistic constraints of adaptive therapy.

(high μ_0) and intense interclonal competition (low α) can preserve the efficacy of adaptive cycles.

These findings suggest that adaptive therapy is not a “one-size-fits-all solution”. Its success relies on the specific balance of tumor kinetics, where the cost of resistance can be leveraged. High-frequency turnover and moderate growth rates favor adaptive protocols, whereas hyper-proliferative tumors require continuous suppression.

4 Conclusion

Non-genetic resistance mechanisms play a critical role in tumor recurrence. A prominent example is resistance mediated by drug-tolerant persister cells (DTPs), a

transient phenotype that allows tumor cells to survive treatment through reversible changes in gene expression, epigenetic modifications, or metabolic reprogramming. Over prolonged exposure, these DTPs may further evolve into stable drug-resistant cells (DRCs). However, the quantitative description of tumor recurrence dynamics and the link between micro-level epigenetic regulation and macro-level tumor population behavior remain poorly understood.

In this study, we developed an agent-based computational framework, combining a mathematical model with a stochastic simulation algorithm, to capture the evolution of cellular epigenetic states and tumor population dynamics during recurrence. To characterize cellular heterogeneity, we introduced three quantitative indicators—sensitivity, proliferative differentiation potential (stemness), and adaptation (resistance)—that directly modulate cell-specific kinetic rates and fitness. To bridge intracellular regulation with population-level outcomes, we defined an inheritance probability function describing the likelihood of daughter cells adopting epigenetic states distinct from their mothers. This framework captures both phenotype transitions and heterogeneity arising from cellular plasticity.

While foundational studies utilizing ordinary differential equations (ODEs) (Kuosmanen et al. 2021; Gevertz et al. 2025) have elegantly demonstrated that phenotypic plasticity alone can drive resistance, they fundamentally rely on mean-field approximations. These macro-scale models assume cells within a compartment (e.g., a tolerant state) are homogeneous. However, drug resistance often originates from the tails of the population distribution—rare subpopulations with extreme epigenetic states (Boumahdi and de Sauvage 2020; Sharma et al. 2010; Rehman et al. 2021). Our agent-based model (ABM) complements these macroscopic continuous frameworks by providing microscopic resolution. By tracking individual cells, our model captures the stochastic emergence of these rate outlier cells, which are often averaged out in deterministic ODE formulations but are critical for predicting the exact timing of relapse.

Crucially, recent single-cell lineage tracing by Whiting et al. (Whiting et al. 2025) has experimentally validated the existence of a continuous transcriptional trajectory during drug adaptation. Our model aligns with this biological reality by defining the cell state as a continuous vector $\mathbf{x} = (x_1, x_2, x_3)$ rather than discrete bins. This allows us to simulate the gradual epigenetic drift along the fitness landscape, offering a mechanistic explanation for the intermediate phenotypes (partial resistance) observed in the clinic.

Parallel efforts in the field have focused on quantifying the dynamics of heterogeneity, for instance, by applying Shannon entropy measures to non-genetic information (Iyer et al. 2025). While providing valuable theoretical metrics for monitoring diversity, our work aims to bridge the gap towards translational application. By explicitly modeling biologically interpretable axes (e.g., x_2 representing stemness/differentiation potential), we extend biological mechanisms into clinical simulation. This structure enables the generation of virtual patient cohorts to test specific dynamic treatment protocols (e.g., tumor-burden-triggered adaptive therapy), demonstrating how continuous epigenetic feedback can be exploited to delay relapse in a personalized manner.

The model was applied to fit experimental data from NSCLC mouse xenografts under EGFR-TKI treatment. Simulations recapitulated tumor growth trajectories and qualitative gene expression changes observed *in vivo*, while also revealing cell-cell epigenetic dynamics and phenotype proportions that are experimentally inaccessible. In particular, the inheritance function parameters were shown to strongly influence plasticity, thereby shaping epigenetic state distributions, phenotype transitions, and tumor growth.

The model further reproduced the reversible nature of DTPs under short-term treatment and the emergence of irreversible DRCs during long-term treatment. This transition was associated with a decline in epigenetic state x_1 , an increase in state x_3 , and the rising fitness of DRCs.

Based on xenograft-fitted parameters, we simulated intermittent and adaptive therapy regimens. Adaptive therapy consistently outperformed continuous dosing, prolonging progression-free survival (PFS) in most virtual patients. However, for patients with intrinsically short PFS, adaptive therapy yielded limited or even adverse outcomes, highlighting the need for personalized treatment optimization.

The critical feature of our multi-scale framework is the explicit mapping between mathematical parameters and biologically actionable mechanisms, which allows for the direct simulation of specific therapeutic interventions. First, the kinetic rate parameters—specifically the maximum proliferation rate $\bar{\beta}$, basal apoptosis rate μ_0 , and differentiation rate κ_0 —serve as quantifiable proxies for cell fate decisions. These rates are not arbitrary variables but can be routinely measured *in vitro* using standard assays such as Ki-67 staining, Annexin V/PI flow cytometry, or live-cell imaging (Mackey 2001; Darzynkiewicz et al. 1994; Kim and Sederstrom 2015). In a clinical context, these parameters represent the primary targets of standard-of-care treatment; for instance, cytotoxic agents like cisplatin and paclitaxel or cytostatic drugs directly modulate $\bar{\beta}$ and μ_0 to induce tumor regression (Shirmanova et al. 2017; Drew et al. 2025; Gupta et al. 2025).

Second, beyond macroscopic growth kinetics, our model captures the molecular regulation of cellular plasticity through the epigenetic inheritance function φ_i . This function governs the probability of phenotypic switching during cell division, a process biologically regulated by epigenetic “writers” and “erasers” such as DNA methyltransferases and histone modifiers. Consequently, the parameter φ_i provides a specific interface for modeling epigenetic therapies. It can be experimentally perturbed using remodeling agents (e.g., DNMT inhibitors like 5-azacytidine or EZH2 inhibitors) (Guler et al. 2017; Ramaiah et al. 2021) or via precise epigenetic editing technologies utilizing CRISPR-Cas9-based epi-editors (Wei et al. 2025; Villiger et al. 2024). By integrating these distinct layers of regulation, our model offers a mechanistic platform to evaluate the efficacy of combination strategies—such as coupling chemotherapy (targeting kinetic rates) with epigenetic therapy (targeting phenotypic plasticity)—to overcome drug resistance.

While the proposed framework offers valuable insights into DTP-mediated resistance, it has limitations. Detailed intracellular signaling networks were abstracted into coarse-grained indices of epigenetic state, which may limit accuracy in reproducing specific datasets. Moreover, the influence of the tumor microenvironment, including

macrophages and cancer-associated fibroblasts (CAFs), was not considered. Future work should integrate signaling pathways and microenvironmental interactions to dissect DTP-driven resistance in greater depth and to refine the design of optimal, patient-specific therapeutic strategies.

Acknowledgements. This work was funded by the National Natural Science Foundation of China (Grant No. 12331018).

Data and Code Availability. The experimental data are available from references. The source code that supports the findings of this study is available from GitHub: <https://github.com/jinzhilei/DTP-Resistance>.

Appendix A Mathematical formulations

In this section, we provide a detailed mathematical derivation of the delay integro-differential equation (DIDE) model, which is derived from the stochastic process described in the main text. This formulation is based on the general framework for heterogeneous stem cell regeneration originally established by [Lei \(2020b\)](#).

Classical cell cycle models, such as the G0 model ([Burns and Tannock 1970](#)), typically assume cell populations are homogeneous. However, single-cell RNA sequencing data have revealed significant heterogeneity in stem cells, characterized by continuous epigenetic states (e.g., transcriptomes, DNA methylation, and histone modifications). Crucially, these states are not perfectly inherited during cell division, leading to dynamic heterogeneity in the progeny. To capture this mathematically, we model the cell population density $Q(t, \mathbf{x})$ using a population balance equation framework. Unlike standard ODEs, this approach accounts for the continuous distribution of phenotypes. The core component is the inheritance probability kernel $p(\mathbf{x}, \mathbf{y})$, which defines the conditional probability that a mother cell with epigenetic state \mathbf{y} produces a daughter cell with state \mathbf{x} . This formulation ensures that population evolution is driven by the interplay between state-dependent proliferation and stochastic inheritance noise.

As illustrated in Fig. 1A, let $s(t, a, \mathbf{x})$ denote the density of proliferating cells at time t with epigenetic state \mathbf{x} and age a , and let $Q(t, \mathbf{x})$ represent the density of resting (G0) cells with state \mathbf{x} . Adopting the notation from the framework in [Lei \(2020a,b\)](#), the system is governed by the following partial differential equations:

$$\frac{\partial s(t, a, \mathbf{x})}{\partial t} + \frac{\partial s(t, a, \mathbf{x})}{\partial a} = -\mu(\mathbf{x})s(t, a, \mathbf{x}), \quad t > 0, 0 < a < \tau(\mathbf{x}), \quad (\text{A1})$$

$$\begin{aligned} \frac{\partial Q(t, \mathbf{x})}{\partial t} &= -\left(\beta(Q(t), \mathbf{x}) + \kappa(\mathbf{x})\right)Q(t, \mathbf{x}) \\ &\quad + 2 \int_{\Omega} s(t, \tau(\mathbf{y}), \mathbf{y})p(\mathbf{x}, \mathbf{y})d\mathbf{y}, \end{aligned} \quad (\text{A2})$$

with the boundary condition for cells entering the proliferative phase:

$$s(t, 0, \mathbf{x}) = \beta(Q(t), \mathbf{x})Q(t, \mathbf{x}). \quad (\text{A3})$$

Here, the total number of cells in the resting phase at time t is

$$Q(t) = \int_{\Omega} Q(t, \mathbf{x}) d\mathbf{x}. \quad (\text{A4})$$

Note that the operator in Eq. (A1) represents the transport of cells through cell cycle age a . The total tumor cell population is given by

$$N(t) = Q(t) + \int_{\Omega} \int_0^{\tau(\mathbf{x})} s(t, a, \mathbf{x}) da d\mathbf{x}. \quad (\text{A5})$$

Equation (A1), coupled with the boundary condition (A3), can be solved using the interaction of characteristic lines (method of characteristics), yielding:

$$s(t, \tau(\mathbf{x}), \mathbf{x}) = \beta(Q_{\tau(\mathbf{x})}(t), \mathbf{x}) Q_{\tau(\mathbf{x})}(t, \mathbf{x}) e^{-\mu(\mathbf{x})\tau(\mathbf{x})}, \quad (\text{A6})$$

where we define the time-delayed terms $Q_{\tau(\mathbf{x})}(t) = Q(t - \tau(\mathbf{x}))$ and $Q_{\tau(\mathbf{x})}(t, \mathbf{x}) = Q(t - \tau(\mathbf{x}), \mathbf{x})$. Substituting (A6) into (A2), we eliminate the age variable a and obtain the following closed delay integro-differential equation for $Q(t, \mathbf{x})$:

$$\begin{aligned} \frac{\partial Q(t, \mathbf{x})}{\partial t} = & -Q(t, \mathbf{x}) \left(\beta(Q(t), \mathbf{x}) + \kappa(\mathbf{x}) \right) \\ & + 2 \int_{\Omega} \beta(Q_{\tau(\mathbf{y})}(t), \mathbf{y}) Q_{\tau(\mathbf{y})}(t, \mathbf{y}) e^{-\mu(\mathbf{y})\tau(\mathbf{y})} p(\mathbf{x}, \mathbf{y}) d\mathbf{y}. \end{aligned} \quad (\text{A7})$$

Equation (A7) represents the deterministic continuum limit corresponding to the stochastic simulation framework used in this study. This type of equation, verified in [Lei \(2020b\)](#) to describe plastic regeneration, allows for the quantitative analysis of tumor relapse dynamics driven by continuous phenotype transitions ([Zhang et al. 2021](#); [Ma et al. 2023](#); [Wang et al. 2025](#)). The specific functional forms of the kinetic rates β, κ, μ , the inheritance kernel $p(\mathbf{x}, \mathbf{y})$, and the drug-induced perturbations are detailed in Section 2.1 of the main text.

Appendix B Reduction to one-dimensional epigenetic state and validation of the agent-based model

To establish the theoretical equivalence between the deterministic framework and the agent-based stochastic simulation, we first simplify the model to a single epigenetic state x_1 . This reduction eliminates dimensionality challenges while retaining the core mechanisms of phenotypic plasticity—specifically, the dependence of proliferation (β) and apoptosis (μ_1) rates on x_1 , and the stochastic inheritance of state during division. The simplified model allows direct numerical integration for comparison with stochastic simulations.

State x_1 affects only the proliferation and apoptosis rates, so Eq. (A7) is rewritten as (we write x_1 as x for simplicity)

$$\frac{\partial Q(t, x)}{\partial t} = -Q(t, x)(\beta(Q, x) + \kappa) + 2 \int_{\Omega} \beta(Q(t - \tau), y) Q(t - \tau, y) e^{-\mu(y)\tau} p(x, y) dy, \quad (\text{B8})$$

where $Q(t, x)$ denotes the population density of resting cells with epigenetic state x at time t , $\tau = 15h$ is the constant cell cycle duration, and κ_0 is the state-independent terminal differentiation rate.

The corresponding kinetic rates are defined as

$$\beta(Q, x) = \bar{\beta} \frac{\theta(x)}{\theta(x) + Q}, \quad \kappa = \kappa_0,$$

where $\theta(x)$ modulates density dependence:

$$\theta(x) = \bar{\theta} \left(1 + a_5 \frac{(a_4 x)^6}{1 + (a_4 x)^6} \right),$$

and apoptosis increases with x via:

$$\mu(x) = \mu_0 \exp(\mu_1(\gamma_1 - x)).$$

The inheritance probability kernel $p(x, y)$ follows a Gamma distributions:

$$p(x, y) = \frac{b(y)^{-a}}{\Gamma(a)} x^{a-1} e^{-x/b(y)}, \quad \text{with } b(y) = \frac{\varphi(y)}{a},$$

where $\varphi(y)$ describes drug-dependent inheritance variance as:

$$\varphi(y) = (\varphi_{10} - Dc_{10}) + (\varphi_{11} - Dc_{11}) \frac{y^{n_1}}{K_1^{n_1} + y^{n_1}}. \quad (\text{B9})$$

To validate the agent-based model, we compared deterministic and stochastic outcomes for Eq. (B8). The deterministic solution was obtained by discretizing $\Omega = [0, 8]$ into 100 bins and solving via finite differences ($\Delta t = 0.1h$). Agent-based stochastic simulations (Algorithm 1) were repeated 3 times with $N(0) = 400$ cells, initialized with $x \sim \mathcal{U}(0, 8)$. Drug was administered from day 50 to 70 ($D = 1$ in Eq. B9). We set the parameter values as

$$\begin{aligned} \bar{\beta} &= 0.10h^{-1}, \quad \bar{\theta} = 1 \times 10^3, \quad \kappa_0 = 0.01h^{-1}, \quad a_4 = 0.25, \quad a_5 = 10, \\ \mu_0 &= 9.0 \times 10^{-3}h^{-1}, \quad \mu_1 = 0.9, \quad \tau = 15h, \quad \gamma_1 = 4.5, \quad a = 50, \\ \varphi_{10} &= 0.7, \quad c_{10} = 0.15, \quad \varphi_{11} = 4.35, \quad c_{11} = 1.5, \quad K_1 = 2.2, \quad n_1 = 2.0, \end{aligned} \quad (\text{B10})$$

in the simulation.

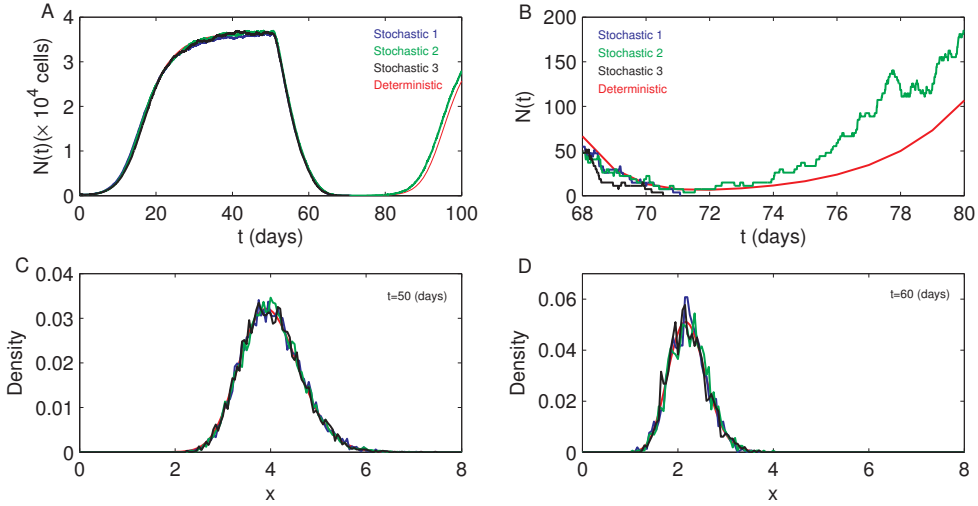


Fig. B1 Validation of agent-based simulation (blue, green, and black) against deterministic IDE solutions (red). **A** Evolution of the total cell number $N(t)$. **B** Zoom-in of $N(t)$ near extinction/relapse. Stochastic runs show divergent outcomes (extinction in 2/3 cases and relapse in 1/3 cases), while the deterministic model predicts recovery. **C-D** Epigenetic state distributions at day 50 (pre-drug) and 60 (on-drug), showing strong agreement between different runs. Parameters are given in (B10); drug administered from day 50 to 70.

Simulation results showed excellent agreement in mean $N(t)$ (Fig. B1A) and state distribution (Fig. B1C-D), confirming the ABM accurately reproduces deterministic dynamics for large populations. However, stochasticity drives divergence when $N(t) < 100$ cells (Fig. B1B): extinction occurs in 2/3 runs due to demographic noise, whereas the deterministic model (lacking such noise) predicts inevitable relapse. This highlights the ABM’s unique value in capturing rare extinction events that are critical for predicting clinical outcomes.

Appendix C Virtual patients and PFS data generation

To capture inter-patient heterogeneity within the cohort, we define a “virtual patient” (VP) as a unique instance of the tumor model characterized by a specific parameter set. Based on the local sensitivity analysis presented in Section 3.5.1, we identified four key parameters— β , κ_0 , α , and μ_0 —that most significantly influence tumor relapse time. Consequently, a VP is represented by the vector $\mathbf{v} = (\bar{\beta}, \kappa_0, \alpha, \mu_0)$, while other parameters remain fixed at their baseline values (Table 3).

The generation of the virtual cohort involves a rejection sampling approach coupled with a Gaussian Mixture Model (GMM), summarized in the following steps:

1. **Baseline Estimation:** We first estimated the baseline parameter vector by fitting the model to the median Progression-Free Survival (PFS) observed in clinical data

(EURTAC trial):

$$\bar{\beta}_{\text{base}} = 0.011, \kappa_{0,\text{base}} = 0.004, \mu_{0,\text{base}} = 0.0013, \alpha_{\text{base}} = 0.95.$$

2. **Parameter Space Construction:** To account for patient variability and biological trade-offs, we introduced two scalar tuning factors, R_1 and R_2 , to perturb the baseline parameters. The candidate parameter space is defined as:

$$\begin{aligned} \bar{\beta} &= \bar{\beta}_{\text{base}} \times R_1 \\ \kappa_0 &= \kappa_{0,\text{base}} \times R_1 \\ \alpha &= \alpha_{\text{base}} \times (0.9 + 0.2R_2), \\ \mu_0 &= \mu_{0,\text{base}} \times (1.4 - 0.8R_2). \end{aligned} \tag{C11}$$

Here, R_1 modulates the overall turnover rate (proliferation and differentiation), while R_2 introduces an inverse correlation between competition strength (α) and intrinsic apoptosis (μ_0), reflecting the cost-of-resistance trade-off.

3. **Sampling and Filtering (Rejection Sampling):** We discretized the domains of R_1 and R_2 to generate 2,000 candidate pairs. Each pair was mapped to a parameter vector \mathbf{v} via Eq. (C11). We then performed stochastic simulations for each candidate vector. A subset of parameters was selected (accepted) only if their simulated tumor recurrence times fell within the confidence interval of the clinical observations.
4. **Distribution Approximation:** The accepted parameter vectors served as training data to fit a multivariate Gaussian Mixture Model (GMM). This continuous probability distribution, denoted as $\mathcal{P}(R_1, R_2)$, characterizes the population-level heterogeneity of the specific cancer subtype.
5. **Virtual Cohort Generation:** Finally, we sampled new cohorts of virtual patients from the learned distribution $\mathcal{P}(R_1, R_2)$. Stochastic simulations were performed on these cohorts under various adaptive therapy protocols to generate the corresponding PFS distributions and evaluate treatment efficacy.

References

Aissa A, Islam A, Ariss M, et al (2021) Single-cell transcriptional changes associated with drug tolerance and response to combination therapies in cancer. *Nat Commun* 12:110162

Arasada R, Shilo K, Yamada T, et al (2018) Notch3-dependent β -catenin signaling mediates egfr tki drug persistence in egfr mutant nsclc. *Nat Commun* 9(1):3198

Balaban NQ, Helaine S, Lewis K, et al (2019) Definitions and guidelines for research on antibiotic persistence. *Nat Rev Microbiol* 17(7):441–448. <https://doi.org/10.1038/s41579-019-0196-3>

Bell CC, Gilan O (2020) Principles and mechanisms of non-genetic resistance in cancer. *Br J Cancer* 122(4):465–472

Bernard S, Bélair J, Mackey MC (2003) Oscillations in cyclical neutropenia: new evidence based on mathematical modeling. *J Theor Biol* 223(3):283–298. [https://doi.org/10.1016/s0022-5193\(03\)00090-0](https://doi.org/10.1016/s0022-5193(03)00090-0)

Boumahdi S, de Sauvage F (2020) The great escape: tumour cell plasticity in resistance to targeted therapy. *Nat Rev Drug Discov* 19(1):39–56

Burns FJ, Tannock IF (1970) On the existence of a G0-phase in the cell cycle. *Cell Prolif* 3(4):321–334

Calderon A, Han C, Karma S, et al (2024) Non-genetic mechanisms of drug resistance in acute leukemias. *Trends Cancer* 10(1):38–51. <https://doi.org/10.1016/j.trecan.2023.09.003>

Chisholm RH, Lorenzi T, Lorz A, et al (2015) Emergence of drug tolerance in cancer cell populations: An evolutionary outcome of selection, nongenetic instability, and stress-induced adaptation. *Cancer Research* 75(6):930–939

Darzynkiewicz Z, Gong J, Traganos F (1994) Analysis of DNA content and cyclin protein expression in studies of DNA ploidy, growth fraction, lymphocyte stimulation, and the cell cycle. *Methods Cell Biol* 41:421–435. [https://doi.org/10.1016/s0091-679x\(08\)61732-x](https://doi.org/10.1016/s0091-679x(08)61732-x)

Drew Y, Zenke FT, Curtin NJ (2025) DNA damage response inhibitors in cancer therapy: lessons from the past, current status and future implications. *Nat Rev Drug Discov* 24(1):19–39. <https://doi.org/10.1038/s41573-024-01060-w>

Feinberg AP, Levchenko A (2023) Epigenetics as a mediator of plasticity in cancer. *Science* 379(6632):eaaw3835

Fischer MM, Blüthgen N (2024) On minimising tumoural growth under treatment resistance. *J Theor Biol* 579:111716

França G, Baron M, King B, et al (2024) Cellular adaptation to cancer therapy along a resistance continuum. *Nature* 631:876–883

Friedman N, Cai L, Xie XS (2006) Linking stochastic dynamics to population distribution: An analytical framework of gene expression. *Phys Rev Lett* 97(16):168302

Gatenby RA, Silva AS, Gillies RJ, et al (2009) Adaptive therapy. *Cancer Res* 69(11):4894–4903

Gevertz J, Greene J, Prosperi S, et al (2025) Understanding therapeutic tolerance through a mathematical model of drug-induced resistance. *npj Syst Biol Appl* 11(30):1–15

Guler GD, Tindell CA, Pitti R, et al (2017) Repression of stress-induced LINE-1 expression protects cancer cell subpopulations from lethal drug exposure. *Cancer*

Cell 32(2):221–237. <https://doi.org/10.1016/j.ccell.2017.07.002>

Gunnarsson E, B.V. M, Foo J (2025) Optimal dosing of anti-cancer treatment under drug-induced plasticity. *npj Syst Biol Appl* 11(98):1–15

Gupta J, Saeed BI, Bishoyi AK, et al (2025) From cell cycle control to cancer therapy: exploring the role of CDK1 and CDK2 in tumorigenesis. *Med Oncol* 42(9):422. <https://doi.org/10.1007/s12032-025-02973-1>

Iyer A, Alva A, Granada AE, et al (2025) Inheritable cell-states shape drug-persister correlations and population dynamics in cancer cells. *PLoS Comp Biol* 21(9):1–26

Jagiella N, Muller B, Muller M, et al (2016) Inferring growth control mechanisms in growing multi-cellular spheroids of nsclc cells from spatial-temporal image data. *PLoS Comp Biol* 12(2):1–39

Kim KH, Sederstrom JM (2015) Assaying cell cycle status using flow cytometry. *Curr Protoc Mol Biol* 111:28.6.1–28.6.11. <https://doi.org/10.1002/0471142727.mb2806s111>

Kolokotroni E, Dionysiou D, Veith C, et al (2016) In silico oncology: Quantification of the in vivo antitumor efficacy of cisplatin-based doublet therapy in non-small cell lung cancer (nsclc) through a multiscale mechanistic model. *PLoS Comp Biol* 12(9):1–43. <https://doi.org/10.1371/journal.pcbi.1005093>

Kuosmanen T, Cairns J, Noble R, et al (2021) Drug-induced resistance evolution necessitates less aggressive treatment. *PLoS Comp Biol* 17(9):1–22

Lei J (2020a) Evolutionary dynamics of cancer: From epigenetic regulation to cell population dynamics–mathematical model framework, applications, and open problems. *Sci China Math* 63(3):411–424

Lei J (2020b) A general mathematical framework for understanding the behavior of heterogeneous stem cell regeneration. *J Theor Biol* 492:110196

Li Y, Liang X, Lei J (2025) Integrating gene regulatory network dynamics with heterogeneous stem cell regeneration. *CSIAM Trans Life Sci* 1(2):320–353

Liau BB, Sievers C, Donohue LK, et al (2017) Adaptive chromatin remodeling drives stem cell plasticity and drug tolerance. *Cell Stem Cell* 20(2):233–246

Lima EABF, Faghihi D, Philley R, et al (2021) Bayesian calibration of a stochastic, multiscale agent-based model for predicting in vitro tumor growth. *PLoS Comp Biol* 17(11):1–35

Ma S, Lei J, Lai X (2023) Modeling tumour heterogeneity of PD-L1 expression in tumour progression and adaptive therapy. *J Math Biol* 86(3):38. <https://doi.org/10.1007/s00285-023-01872-1>

Mackey MC (2001) Cell kinetic status of haematopoietic stem cells. *Cell Prolif* 34(2):71–83. <https://doi.org/10.1046/j.1365-2184.2001.00195.x>

Marine JC, Dawson SJ, Dawson MA (2020) Non-genetic mechanisms of therapeutic resistance in cancer. *Nat Rev Cancer* 20(12):743–756. <https://doi.org/10.1038/s41568-020-00302-4>

McClatchy DM, Willers H, Hata AN, et al (2020) Modeling resistance and recurrence patterns of combined targeted-hemoradiotherapy predicts benefit of shorter induction period. *Cancer Research* 80(22):5121–5133

McDonald PC, Dedhar S (2024) Persister cell plasticity in tumour drug resistance. *Semin Cell Dev Biol* 156:1–10. <https://doi.org/10.1016/j.semcd.2023.11.003>

Nie M, Chen N, Pang H, et al (2022) Targeting acetylcholine signaling modulates persistent drug tolerance in EGFR-mutant lung cancer and impedes tumor relapse. *J Clin Invest* 132(20):e160152

Probst A, Dunleavy E, Almouzni G (2009) Epigenetic inheritance during the cell cycle. *Nat Rev Mol Cell Biol* 10(3):192–206

Ramaiah MJ, Tangutur AD, Manyam RR (2021) Epigenetic modulation and understanding of HDAC inhibitors in cancer therapy. *Life Sci* 277:119504. <https://doi.org/10.1016/j.lfs.2021.119504>

Rambow F, Rogiers A, Marin-Bejar O, et al (2018) Toward minimal residual disease-directed therapy in melanoma. *Cell* 174(4):843–855. <https://doi.org/10.1016/j.cell.2018.06.025>

Ramirez M, Rajaram S, Steininger R, et al (2016) Diverse drug-resistance mechanisms can emerge from drug-tolerant cancer persister cells. *Nat Commun* 7:10690

Rehman SK, Haynes J, Collignon E, et al (2021) Colorectal cancer cells enter a diapause-like DTP state to survive chemotherapy. *Cell* 184(1):226–242.e21

Reyes M, Urra H, Peña Oyarzún D (2025) Evaluating the link between periodontitis and oral squamous cell carcinoma through Wnt/β-catenin pathway: a critical review. *Front Oral Health* 6:1575721. <https://doi.org/10.3389/froh.2025.1575721>

Rosell R, Carcereny E, Gervais R, et al (2012) Erlotinib versus standard chemotherapy as first-line treatment for European patients with advanced EGFR mutation-positive non-small-cell lung cancer (EURTAC): a multicentre, open-label, randomised phase 3 trial. *Lancet Oncol* 13(3):239–246. [https://doi.org/10.1016/S1470-2045\(11\)70393-X](https://doi.org/10.1016/S1470-2045(11)70393-X)

Shahrezaei V, Swain PS (2008) Analytical distributions for stochastic gene expression. *Proc Natl Acad Sci USA* 105(45):17256–61

Sharma SV, Lee DY, Li B, et al (2010) A chromatin-mediated reversible drug-tolerant state in cancer cell subpopulations. *Cell* 141(1):69–80. <https://doi.org/10.1016/j.cell.2010.02.027>

Shirmanova MV, Druzhkova IN, Lukina MM, et al (2017) Chemotherapy with cisplatin: insights into intracellular pH and metabolic landscape of cancer cells in vitro and in vivo. *Sci Rep* 7(1):8911. <https://doi.org/10.1038/s41598-017-09426-4>

Straussman R, Morikawa T, Shee K, et al (2012) Tumour micro-environment elicits innate resistance to raf inhibitors through hgf secretion. *Nature* 487:500–504

Villiger L, Joung J, Koblan L, et al (2024) CRISPR technologies for genome, epigenome and transcriptome editing. *Nat Rev Mol Cell Biol* 25(6):464–487. <https://doi.org/10.1038/s41580-023-00697-6>

Wang S, Lei J, Zou X, et al (2025) Integrating multiscale mathematical modeling and multidimensional data reveals the effects of epigenetic instability on acquired drug resistance in cancer. *PLoS Comput Biol* 21(2):e1012815. <https://doi.org/10.1371/journal.pcbi.1012815>

Wei Y, Sun J, Zhu R (2025) CRISPR-epigenetic crosstalk: From bidirectional regulation to therapeutic potential. *Comput Struct Biotechnol J* 27:4496–4504. <https://doi.org/10.1016/j.csbj.2025.10.031>

Whiting FJH, Mossner M, Gabbett C, et al (2025) Quantitative measurement of phenotype dynamics during cancer drug resistance evolution using genetic barcoding. *Nat Commun* 16:5282

Zhang C, Shao C, Jiao X, et al (2021) Individual cell-based modeling of tumor cell plasticity-induced immune escape after CAR-T therapy. *Comput Syst Oncol* 1:e21029

Zheng Y, Bao J, Zhao Q, et al (2018) A spatio-temporal model of macrophage-mediated drug resistance in glioma immunotherapy. *Mol Cancer Ther* 17(4):814–824